Modeling the Effects of Strand Surface Bulging and Mechanical Softreduction on the Macrosegregation Formation in Steel Continuous Casting

JOSEF DOMITNER, MENGHUAI WU, ABDELLAH KHARICHA, ANDREAS LUDWIG, BERNHARD KAUFMANN, JÜRGEN REITER, and THOMAS SCHADEN

Positive centerline macrosegregation is an undesired casting defect that frequently occurs in the continuous casting process of steel strands. Mechanical softreduction (MSR) is a generally applied technology to avoid this casting defect in steel production. In the current paper, the mechanism of MSR is numerically examined. Therefore, two 25-m long horizontal continuous casting strand geometries of industrial scale are modeled. Both of these strand geometries have periodically bulged surfaces, but only one of them considers the cross-section reduction due to a certain MSR configuration. The macrosegregation formation inside of these strands with and without MSR is studied for a binary Fe-C-alloy based on an Eulerian multiphase model. Comparing the macrosegregation patterns obtained for different casting speed definitions allows investigating the fundamental influence of feeding, bulging and MSR mechanisms on the formation of centerline macrosegregation.

I. INTRODUCTION

IN recent years, continuous casting has become the major manufacturing method for semi-finished steel products like slabs, billets, or blooms. Many efforts have been made to avoid macrosegregation formation at the centerline of these products during solidification. Particularly positive centerline macrosegregation leads to problems during the succeeding forming processes and to inhomogeneous mechanical product properties. Hence, reducing this casting defect brings an essential quality improvement. Since macrosegregation cannot be removed from the solidified products, controlling its formation immediately during the casting process is crucial to obtain the required steel quality. Industrial practice has shown that mechanical softreduction (MSR) represents an effective technology to achieve this.[1–7] To operate MSR facilities successfully requires a deep understanding of the macrosegregation forma-tion mechanisms inside of the strand. Since experimental plant trials are usually time-consuming and expensive, detailed numerical simulations become increasingly important to understand the phenomenon of macroseg-regation formation.

Macrosegregation formation is related to relative motion between the solid phase and the melt inside of the cast product. For example, thermal, solutal, or forced convection, shrinkage-induced feeding and solid deformation may cause relative motion between the phases.[8,9] Flemings et al.[10,11] developed analytic expressions to describe the general influence of different solidification variables on the formation of macroseg-gation in castings. The analytical predictions were also verified by experiments, which illustrated that the flow of enriched liquid to feed volume shrinkage due to solidification or to thermal contractions can cause macrosegregations.[12] In continuous strand casting, deformation of the solid strand shell was identified to cause the formation of positive centerline segrega-tion.[13–18] Due to the high metallostatic pressure of the liquid melt inside of the strand, the thin shell is bulged between adjacent guiding rolls. With advancing solidification, the shell thickness increases and therefore this unfavorable effect decreases. To diminish unfavor-able formation of positive centerline segregation, the melt flow caused by bulging inside the strand must be controlled. First fundamental numerical simulations covering the topic of bulging were conducted by Miyazawa and Schwerdtfeger.[13] Later, the work was extended by Kajitani et al.[15] using a simulation model comprising five roll pairs instead of only a single pair. Mayer et al.[17,18] investigated macrosegregation formation due to shrinkage feeding and strand surface

JOSEF DOMITNER, Ph.D. Student, ABDELLAH KHARICHA, Senior Scientist, and ANDREAS LUDWIG, Professor, are with the Chair of Simulation and Modeling of Metallurgical Processes, University of Leoben, 8700 Leoben, Austria. Contact e-mail: josef.domitner@unileoben.ac.at MENGHUAI WU, Associate Profes-sor, is with the Chair of Simulation and Modeling of Metallurgical Processes, University of Leoben, and also with the Christian Doppler Laboratory for Advanced Process Simulation of Solidification and Melting, University of Leoben. BERNHARD KAUFMANN, Senior Project Manager R&D, is with the voestalpine Stahl GmbH, 4020 Linz, Austria. JÜRGEN REITER, Project Manager R&D, is with the voestalpine Stahl Donawitz GmbH & Co KG, 8700 Leoben, Austria. THOMAS SCHADEN, Metallurgist, is with the Siemens VAI Metals Technologies GmbH & Co, 4031 Linz, Austria.
Manuscript submitted September 25, 2012.
Article published online October 24, 2013

bulging based on an academic model geometry of 9 m length considering 101 rolls. A similar geometry was used by the current authors to study the principal of MSR in slab casting.[19] However, surface bulging within the MSR zone was not considered in that model. Nevertheless, compared to industrial continuous casting plant dimensions all of the mentioned strand models were pretty small.

For the presented work, a 25-m long and 285-mm thick full scale cast strand was modeled to investigate macrosegregation formation in continuous casting at industrial scale for a binary Fe-C-alloy. Both, the influence of bulging on the formation as well as the effect of MSR on the reduction of centerline macrosegregation were considered in the model. Strand surface bulging within the MSR zone was also modeled. To perform the simulations, the commercial software package FLUENT (ANSYS, Inc., Canonsburg, PA) was used. The meshed strand geometries were generated with the preprocessing tool GAMBIT (ANSYS, Inc.).

The calculations were performed at an Intel® (Intel, Corp., Santa Clara, CA) Nehalem cluster. For each calculation, one cluster node, consisting of two Intel® Xeon® X5570 quad-core CPUs, was used. The DDR3 main memory of each cluster node had a size of 24 GB and a bus speed of 1333 MHz; each core had a clock speed of 2.93 GHz, a cache size of 8 MB and a bus speed of 6.4 GT s^{-1} (3200 MHz). For each simulation, the runtime required to reach steady state was approximately 1 month.

II. NUMERICAL MODEL

An Eulerian two-phase model was utilized to examine macrosegregation formation inside of the cast strand. It is a simplified version of the three-phase volume-averaging solidification model which was developed by Wu and Ludwig[20–22] and which is based on the work of Beckermann and co-workers.[23,24] The model of Wu and Ludwig describes three main phases occurring generally during solidification processes: the melt, columnar dendrites and equiaxed crystals. The two phases considered in the current work are the melt ("liquid") and the columnar dendrites ("solid") growing from the strand surface toward its center. The equiaxed dendrites are not considered in order to reduce the calculation time. This simplification is reasonable, because the equiaxed phase does not play the important role in continuous slab casting as it does in continuous bloom casting or in ingot casting for example. Since solidification of a binary alloy is modeled, each of both phases, liquid and solid, contains two species, iron and carbon.

A. General Conservation Equations

In the following, the basic conservation equations of mass, momentum, species, and enthalpy are summarized. These conservation equations used in the present simulations are solved numerically for each phase, liquid (index "L") and solid (index "S"). However, the motion of the solid phase is predefined analytically.

1. Mass conservation

$$\frac{\partial}{\partial t}(f_L \rho_L) + \nabla \cdot (f_L \rho_L \vec{v}_L) = M_{SL} \qquad [1]$$

$$\frac{\partial}{\partial t}(f_S \rho_S) + \nabla \cdot (f_S \rho_S \vec{v}_S) = M_{LS} \qquad [2]$$

In Eqs. [1] and [2], f_L and f_S are the volume fractions of the solid and the liquid phase, respectively. Adding up of both fractions results in unity. ρ_L and ρ_S are the mass densities, $\vec{v}_L$ and $\vec{v}_S$ represent the velocity vectors of both phases. Since the model description in this work is based on a two-dimensional Cartesian coordinate system, each of these vectors comprises a x- and a y-velocity component. The exchange term M_{SL} describes the net mass transfer rate from the solid to the liquid phase, whereas the exchange term M_{LS} quantifies the transfer rate into the opposite direction. Equation [3] is used to calculate both exchange terms:

$$M_{SL} = -M_{LS} = -v_{r_1} \rho_S S_{V,T} \Phi. \qquad [3]$$

In Eq. [3], v_{r_1} is the growth velocity of the columnar dendrites in thickness direction. Since it is difficult to describe the complex morphology of real dendritic structures analytically, the dendrites are approximated with cylindrical shapes and constant primary arm spacings λ_1, as shown in Figure 1(a).

In the current model, solidification is governed by diffusion (diffusion coefficient D_L) inside the liquid phase due to a difference between the species concentration at the cylindrical solid–liquid interface C_L^* and the species concentration in the surrounding melt C_L, as shown schematically in Figure 1(b). Diffusion inside the solid phase is neglected in the current model. Hence, v_{r_1} is expressed with Eq. [4]:

$$v_{r_1} = \frac{dr_1}{dt} = \frac{D_L}{r_1} \frac{C_L^* - C_L}{C_L^* - C_S^*} \left(\ln \frac{r_\infty}{r_1} \right)^{-1}. \qquad [4]$$
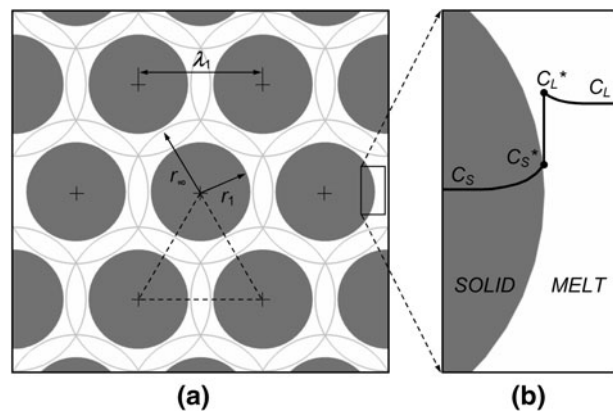
Fig. 1—(a) Geometrical relationships between the dendrite trunk radius and the primary dendrite arm spacing for a regularly staggered alignment of cylindrically shaped dendrites; (b) schematic of a typical concentration pile-up directly at the solidification interface.

In Eqs. [5] and [6], the species concentrations C_L^* and C_S^* at the solidification interface are calculated with a constant partition coefficient k and a constant liquidus slope m. In Eq. [5], T_L is the liquid phase temperature and T_m^{Fe} is the melting temperature of pure iron:

$$C_L^* = \frac{T_L - T_m^{Fe}}{m} \qquad [5]$$

$$C_S^* = kC_L^*. \qquad [6]$$

Assuming a staggered alignment of the columnar dendrites, Eq. [7] is used to calculate the dendrite trunk radius r_1. This equation is derived from simple geometrical relationships between r_1 and λ_1, which are schematically illustrated in Figure 1(a). That also applies to Eq. [8], wherein r_∞ is the radius a solidifying dendrite could theoretically reach inside of the given hexagonal solidification pattern, if the melt would not be exhausted before:

$$r_1 = \lambda_1 \left(\frac{\sqrt{3}f_S}{2\pi} \right)^{0.5} \qquad [7]$$

$$r_\infty = \frac{\lambda_1}{\sqrt{3}}. \qquad [8]$$

The total area-volume ratio $S_{V,T}$, which is introduced in Eq. [9] relates the surface area of the cylindrical dendrites A_{SL} to the total volume V_T, including the solid and the liquid phase:

$$S_{V,T} = \frac{A_{SL}}{V_T} = \frac{4\pi r_1}{\sqrt{3}\lambda_1^2}. \qquad [9]$$

If r_1 is larger than $\lambda_1/2$, the dendrites can not be treated as ideally shaped cylinders, because with ongoing solidification adjacent dendrite trunks will overlap each other. The impingement factor Φ, which is given in Eq. [10] accounts for this overlapping at high solid fractions:

$$\begin{aligned} r_1 \leq \frac{\lambda_1}{2}: \quad & \Phi = 1 \\ r_1 > \frac{\lambda_1}{2}: \quad & \Phi = (1 - f_S)\left(1 - \frac{\pi}{2\sqrt{3}} \right)^{-1}. \end{aligned} \qquad [10]$$

According to the previous equation, two regimes are distinguished to define Φ. While $\Phi = 1$ for all dendrite radii smaller than $\lambda_1/2$, the impingement factor decreases linearly for dendrite radii larger than $\lambda_1/2$, until $\Phi = 0$ at $f_S = 1$.

2. *Momentum conservation*

$$\begin{aligned} &\frac{\partial}{\partial t}(f_L \rho_L \vec{v}_L) + \nabla \cdot (f_L \rho_L \vec{v}_L \times \vec{v}_L) \\ &= -f_L \nabla p + \nabla \cdot \left(\eta_L f_L \left(\nabla \cdot \vec{v}_L + (\nabla \cdot \vec{v}_L)^T \right) \right) \\ &+ f_L \rho_L \vec{g} - \vec{V}_{LS}^M - \vec{V}_{LS}^D \end{aligned} \qquad [11]$$

As already mentioned, the momentum conservation equation for the solid phase is not solved, because the solid motion is predefined in the current model. The velocity pattern of the liquid phase is described by the Navier–Stokes equation, Eq. [11], wherein p is the static pressure and η_L represents the dynamic viscosity of the melt. The gravity acceleration $\vec{g}$ is not considered in the model. As expressed with Eq. [12], $\vec{V}_{LS}^M$ quantifies the momentum exchange due to the phase change from liquid to solid:

$$\vec{V}_{LS}^M = \vec{v}_L M_{LS}. \qquad [12]$$

$\vec{V}_{LS}^D$ quantifies the momentum exchange caused by hydrodynamic interaction between the solid phase and interdendritic liquid flow, the so-called "drag force". As denoted with Eq. [13], $\vec{V}_{LS}^D$ is inverse proportional to the permeability K of the mushy zone:

$$\vec{V}_{LS}^D = \frac{\eta_L}{K}(1 - f_S)^2(\vec{v}_L - \vec{v}_S) \qquad [13]$$

$$K = 0.0006\lambda_1^2 \frac{(1 - f_S)^3}{f_S^2}. \qquad [14]$$

Equation [14] describes the isotropic permeability on the entire solid fraction range.[25] However, deep inside the mushy zone at high solid fractions the permeability is quite low, and therefore the feeding flow due to solidification shrinkage is completely prevented. Actually, this results in forming local pores or in deforming the already solidified dendrites to compensate the volume change caused by solidification shrinkage. Since both of these mechanisms are not included in the current solidification model, the so-called "simplified porosity model" (SPM) is introduced instead.[17] Beyond the predefined critical solid fraction f_S^{SPM} no relative motion between the solid dendrites and the remaining interdendritic melt occurs. The SPM implies that the density of the solid forming at $f_S > f_S^{SPM}$ deep inside the mushy zone is the same as the density of the melt, ρ_L. According to this assumption, the average density $\bar{\rho}_S$ of the solid formed below and beyond f_S^{SPM} is calculated with Eq. [15]:

$$\bar{\rho}_S = \frac{\rho_S f_S^{SPM} + \rho_L (1 - f_S^{SPM} - f_L)}{1 - f_L} \qquad [15]$$

3. *Species conservation*

$$\frac{\partial}{\partial t}(f_L \rho_L C_L) + \nabla \cdot (f_L \rho_L \vec{v}_L C_L) = C_{SL}^M + C_{SL}^D \qquad [16]$$

$$\frac{\partial}{\partial t}(f_S \rho_S C_S) + \nabla \cdot (f_S \rho_S \vec{v}_S C_S) = C_{LS}^M + C_{LS}^D \qquad [17]$$

In Eqs. [16] and [17], C_L and C_S are the volume-averaged concentrations in the liquid and the solid, respectively. Since a simple carbon alloyed steel is investigated in the

current simulations, C_L and C_S characterize the carbon concentrations within liquid and solid. Species exchange is modeled according to the simplified linear phase diagram of a binary Fe-C steel using the constant distribution coefficient k. The species transfer terms C_{SL}^M and C_{LS}^M due to phase change are calculated with Eq. [18]:

$$C_{SL}^M = -C_{LS}^M = -M_{LS} k C_L^*.$$ [18]

However, the contributions of the diffusive species transfer rates C_{SL}^D and C_{LS}^D are neglected, because the influence of diffusion as well as back diffusion at macroscopic length scale are not considered in the current model.

4. Enthalpy conservation

$$\frac{\partial}{\partial t}(f_L \rho_L h_L) + \nabla \cdot (f_L \rho_L \vec{v}_L h_L)$$
$$= \nabla \cdot (f_L k_L \nabla \cdot T_L) + Q_L^M + Q_{SL}^D$$ [19]

$$\frac{\partial}{\partial t}(f_S \rho_S h_S) + \nabla \cdot (f_S \rho_S \vec{v}_S h_S)$$
$$= \nabla \cdot (f_S k_S \nabla \cdot T_S) + Q_S^M + Q_{LS}^D$$ [20]

In Eqs. [19] and [20], h_L and h_S are the enthalpies, T_L and T_S the temperatures of the solid and the liquid phase, respectively. The energy exchanges Q_{SL}^D and Q_{LS}^D due to heat transfer are calculated with Eq. [21]. Therein, H^* represents the volumetric heat transfer coefficient between the two phases. Furthermore, the phase change energy source terms Q_S^M and Q_L^M are considered using Eqs. [22] and [23]. ΔH_m is the latent heat of fusion:

$$Q_{SL}^D = -Q_{LS}^D = -H^*(T_L - T_S)$$ [21]

$$Q_S^M = M_{LS}(\Delta H_m f_S - h_S)$$ [22]

$$Q_L^M = M_{LS}(\Delta H_m f_L - h_L).$$ [23]

B. Model Geometry

The investigated horizontal continuous casting strand has a total length of $l = 25$ m and an overall thickness of $w = 285$ mm. Neglecting the influence of gravity on the segregation formation enables to model only one half of the symmetric strand. Therefore, the thickness of the calculation domain is reduced to $w/2 = 142.5$ mm in the created simulation model. The specifications of the strand model geometries are summarized in Table I.

Although the performed simulations base on the same Eulerian two-phase model, two different model geometries (G1 and G2) are considered:

- G1: considers bulging between the guiding rolls
- G2: considers bulging and mechanical softreduction

Both model geometries are similar. G2 can be construed as extended modification of G1, having an additional

Table I. Specifications of the Strand Geometries

Strand Length	l	25,000 mm
Overall Strand Thickness	w	285 mm
Softreduction Height	s	4.65 mm
Mold Length	q	820 mm
Initial Bulging Height	d_0	0.8 mm
Distance Between Guiding Rolls	h	300 mm
Total Number of Rolls	n	75
Melt Meniscus Coordinate	x_{-1}	−820 mm
Bulging Start Coordinate	x_0	0 mm
MSR Start Coordinate	x_1	17,850 mm
Bulging & MSR End Coordinate	x_2	22,500 mm
Strand End Coordinate	x_3	24,180 mm

cross-section reduction due to MSR. Each of these two-dimensional model geometries is subdivided into four zones:

- Z1: $x_{-1} < x \leq x_0$ mold zone
- Z2: $x_0 < x \leq x_1$ secondary cooling zone
- Z3: $x_1 < x \leq x_2$ softreduction zone
- Z4: $x_2 < x \leq x_3$ strand end zone

While the surfaces of Z1 and Z4 are totally flat, those of Z2 and Z3 are sinusoidally waved due to periodical surface bulging between adjacent strand guiding rolls. The wave troughs indicate the position of the guiding rolls, which are arranged at a constant horizontal spacing h. Based on the initial bulging amplitude d_0 at the beginning of zone Z2, the amplitude decreases linearly toward zero at the end of zone Z3. Only for model geometry G2 the strand thickness w is continuously reduced within Z3 according to the predefined MSR height s, but for geometry G1 w is constant within Z3. The contour of the strand surface is described analytically using the following equations:

$$y^{surf,Z1} = \frac{w}{2}$$ [24]

$$y^{surf,Z2} = \frac{w}{2} - \frac{d_0}{2}\left(1 - \frac{(x-x_0)}{nh}\right)\left(\cos\left(\frac{2\pi(x-x_0)}{h}\right) - 1\right)$$ [25]

$$y^{surf,Z3} = y^{surf,Z2} - \frac{s}{2}\left(\frac{x-x_1}{x_2-x_1}\right)$$ [26]

$$y^{surf,Z4} = \frac{w-s}{2}.$$ [27]

In Eqs. [24] to [27], y^{surf} represents the coordinate of the strand surface in the model zones Z1 to Z4, depending on the strand length coordinate x. Notice that the second term of Eq. [26] is only valid for model geometry G2, where the strand thickness is reduced due to MSR.

C. Solid Phase Velocity Definitions

In the current model, the motion of the solid phase is defined analytically according to the surface contour of the cast strand. Particularly, the solid phase velocity

normal to the cast direction is directly related to the surface contour.

1. Casting velocity and pull velocity

The casting velocity v^{cast} is the velocity of the solid strand shell at the outlet of the mold, zone Z1. The pull velocity v^{pull} is the velocity of the solid strand at the end of the MSR segment, zone Z3. Both, v^{cast} as well as v^{pull}, are always parallel to the cast direction x. In the performed simulations, all solid phase velocity definitions are basically related to v^{cast}.

Measurements performed in plant trails at voestalpine Stahl GmbH have shown that the casting velocity does not increase significantly, although the thickness of the strand decreases.[28] That implies that the velocity is constant inside as well as at the outlet of the MSR zone. However, one cannot exclude that slight velocity variations having also an influence on the macrosegregation formation are overlooked in the industrial speed measurements. Neglecting these uncertainties means that

$$v^{pull} = v^{cast}. \quad [28]$$

Applying MSR in continuous casting leads to a slight reduction of the initial strand thickness w. According to the continuity law for incompressible materials, this results in a higher strand velocity at the outlet of the MSR zone Z3:

$$v^{pull} = v^{cast}\left(\frac{w}{w-s}\right). \quad [29]$$

Equation [29] implies that the strand is fully solid in its cross-section and the strand width stays constant while the thickness is reduced. However, normally a core of remaining liquid still exists at the strand center if MSR is applied. Thus, internal melt flow can partially compensate the volume change due to strand thickness reduction. Both, Eqs. [28] and [29], deliver two distinct values and v^{pull} is assumed to have an actual value somewhere in between. However, due to a lack of exact velocity determination the influence of both velocity definitions are considered for model geometry G2 ($\rightarrow$ simulation cases G2-I and G2-II). Table II gives an overview about the main mechanisms taken into consideration in the three simulation cases G1, G2-I, and G-II.

Based on v^{cast}, v^{pull} and on the MSR zone geometry, the so-called "MSR factor" γ was introduced by Wu et al.[19] to quantify the MSR configuration with one single number:

$$\gamma = \frac{v^{pull}\frac{w-s}{w} - v^{cast}}{x_2 - x_1}. \quad [30]$$

According to γ, which has the sign and the unit of $\nabla \cdot \vec{v}_S$, three general MSR configurations are distinguished:

- $\gamma < 0$ ($\nabla \cdot \vec{v}_S < 0$): The volume of the MSR zone is compressed, because more solid is entering than leaving the zone. However, in the current model the solid phase deformation is assumed to be volume conserving and

Table II. Mechanisms Considered in the Simulation Cases

Simulation Case	G1	G2-I	G2-II
Surface Bulging	yes	yes	yes
Mechanical Softreduction (MSR)	no	yes	yes
Varying Solid Velocity in x-direction	no	no	yes

therefore divergence-free after reaching the predefined value of f_S^{zero}, the so-called zero-strength solid fraction. Hence, the domain of $f_S > f_S^{zero}$ is incompressible. Accordingly, compression caused by MSR can only occur inside the dendritic mushy zone, where the interdendritic space is reduced and the melt is squeezed out. This applies to simulation case G2-I.

- $\gamma = 0$ ($\nabla \cdot \vec{v}_S = 0$): No solid phase divergence occurs within the entire MSR zone, neither inside the totally solid domain nor in the two-phase mushy zone. This applies to simulation case G2-II, where the solid phase deformation due to MSR is completely divergence-free.

- $\gamma > 0$ ($\nabla \cdot \vec{v}_S > 0$): The volume inside of the MSR zone expands, because more solid is leaving than entering the zone. As a consequence, the lack of solid phase volume is compensated by melt being drawn from elsewhere into the enlarging interdendritic space.

Among the three simulation cases of Table II, G2-II represents the most general case. Hence, the solid phase velocity definitions described in the following sections are focussed on G2-II, where $v^{cast} < v^{pull}$ and $\gamma = 0$.

2. Solid phase velocity at the strand surface

(a) Velocity component parallel to the cast direction: In the case of increasing strand velocity, $v_{S,x}^{surf}$ depends on the strand length coordinate x. Within zones Z1 and Z2, $v_{S,x}^{surf}$ is equal to the constant casting speed v^{cast}, Eq. [31]. Then $v_{S,x}^{surf}$ linearly increases in zone Z3 until v^{pull} is reached, Eq. [32], which finally stays constant in strand end zone Z4, Eq. [33]:

$$v_{S,x}^{surf,Z1} = v_{S,x}^{surf,Z2} = v^{cast} \quad [31]$$

$$v_{S,x}^{surf,Z3} = v^{cast} + \left(\frac{x - x_1}{x_2 - x_1}\right)(v^{pull} - v^{cast}) \quad [32]$$

$$v_{S,x}^{surf,Z4} = v^{pull}. \quad [33]$$

(b) Velocity component perpendicular to the cast direction: For model zones Z1 to Z4, the strand surface velocity perpendicular to the cast direction, $v_{S,y}^{surf}$, is calculated from the first derivative of Eqs. [24] to [27]:

$$v_{S,y}^{surf,Z1-Z4} = v_{S,x}^{surf,Z1-Z4}\frac{\partial y^{surf,Z1-Z4}}{\partial x}. \quad [34]$$

Since the modeled strand surface is horizontal and totally flat at the mold zone Z1 as well as at the strand end zone Z4, no surface velocity components in y-direction occur at these zones, Eqs. [35] and [38]. However, due to the sinusoidally waved surfaces of zones Z2 and Z3, the relationships given in Eqs. [36] and [37] are achieved to describe the solid phase velocity in y-direction at the strand surface, $v_{S,y}^{surf}$:

$$v_{S,y}^{surf,Z1} = 0 \qquad [35]$$

$$v_{S,y}^{surf,Z2} = v_{S,x}^{surf,Z2}\left(\left(\frac{d_0}{2nh}\left(\cos\left(\frac{2\pi(x-x_0)}{h}\right)-1\right)\right) + \frac{d_0\pi}{h}\sin\left(\frac{2\pi(x-x_0)}{h}\right)\left(1-\frac{(x-x_0)}{nh}\right)\right) \qquad [36]$$

$$v_{S,y}^{surf,Z3} = v_{S,x}^{surf,Z3}\left(\left(\frac{d_0}{2nh}\left(\cos\left(\frac{2\pi(x-x_0)}{h}\right)-1\right)\right) + \frac{d_0\pi}{h}\sin\left(\frac{2\pi(x-x_0)}{h}\right)\left(1-\frac{(x-x_0)}{nh}\right) - \frac{s}{2(x_2-x_1)}\right) \qquad [37]$$

$$v_{S,y}^{surf,Z4} = 0. \qquad [38]$$

In Figure 2, y^{surf}, $v_{S,x}^{surf}$ and $v_{S,y}^{surf}$ are plotted along the entire strand length for all of the four model zones. According to Figure 2(a), it is obvious that the surfaces of model geometries G1 (bulging geometry) and G2 (MSR geometries I and II) differ only in zones Z3 and Z4. As shown in Figure 2(b) the velocity component $v_{S,x}^{surf}$ is identical for G1 and for G2-I. In both cases, $v_{S,x}^{surf}$ is constant along the entire strand length. However, $v_{S,x}^{surf}$ is different for G2-II, because $v_{S,x}^{surf}$ increases at the MSR zone Z3. At first sight, the velocity profile depicted in Figure 2(c) seems to be identical for geometries G1 and G2, but a detailed examination indicates a different sinusoidal $v_{S,y}^{surf}$-profile at the MSR zone. There, $v_{S,y}^{surf}$ is slightly smaller for G2 than for G1, which is due to the cross-section reduction at the MSR zone.

3. *Solid phase velocity inside of the strand*

(a) Velocity component parallel to the cast direction: The internal solid phase velocity parallel to the cast direction, $v_{S,x}$, is equal to the corresponding solid phase velocity $v_{S,x}^{surf}$ at the strand surface. This definition is valid for each of the model zones, Z1 to Z4:

$$v_{S,x}^{Z1-Z4} = v_{S,x}^{surf,Z1-Z4}. \qquad [39]$$

(b) Velocity component perpendicular to the cast direction: In model regions where $f_S > f_S^{zero}$, the velocity pattern must be treated as divergence-free to prevent undesired relative motion between the liquid and the solid, which would lead to unphysical macrosegregation formation. Hence, the condition of Eq. [40] must be fulfilled, which can be rewritten to Eq. [41] for a 2D problem considering constant solid phase density ρ_S:

$$\nabla \cdot (\rho_S \vec{v}_S) = 0 \qquad [40]$$

$$\frac{\partial v_{S,y}^{Z1-Z4}}{\partial y} = -\frac{\partial v_{S,x}^{Z1-Z4}}{\partial x}. \qquad [41]$$

For simulation case G2-II, the solid velocity in the cast direction, $v_{S,x}$, is only constant within zones Z1, Z2, and Z4. Hence, the first derivative of Eqs. [31] and [33] according to the right-hand side of Eq. [41] results in zero:

$$\frac{\partial v_{S,x}^{Z1}}{\partial x} = 0; \quad \frac{\partial v_{S,x}^{Z2}}{\partial x} = 0; \quad \frac{\partial v_{S,x}^{Z4}}{\partial x} = 0. \qquad [42]$$

Thus, the internal solid phase velocity perpendicular to the cast direction, $v_{S,y}$, is equal to the corresponding surface velocity $v_{S,y}^{surf}$ within the three zones Z1, Z2, and Z4:

$$v_{S,y}^{Z1} = v_{S,y}^{surf,Z1}; \quad v_{S,y}^{Z2} = v_{S,y}^{surf,Z2}; \quad v_{S,y}^{Z4} = v_{S,y}^{surf,Z4}. \qquad [43]$$

However, within MSR zone Z3, $v_{S,x}$ depends on the strand coordinate in x-direction. Therefore, the first derivation of Eq. [32] according to the right-hand side of Eq. [41] delivers:

$$\frac{\partial v_{S,x}^{Z3}}{\partial x} = \frac{v^{pull} - v^{cast}}{x_2 - x_1}, \qquad [44]$$

which is then integrated to obtain $v_{S,y}$:

$$v_{S,y}^{Z3} = -\int \frac{\partial v_{S,x}^{Z3}}{\partial x} dy \qquad [45]$$

$$v_{S,y}^{Z3} = C - \left(\frac{v^{pull} - v^{cast}}{x_2 - x_1}\right)y. \qquad [46]$$

In zone Z3, the integration constant C is determined by the surface profile y^{surf} (Eq. [26]) and by the surface velocity $v_{S,y}^{surf}$ (Eq. [37]):

$$C = v_{S,y}^{surf,Z3} + \left(\frac{v^{pull} - v^{cast}}{x_2 - x_1}\right)y^{surf,Z3}. \qquad [47]$$

Finally, combining Eqs. [46] and [47] delivers the expression which defines $v_{S,y}^{Z3}$, the solid velocity perpendicular to the cast direction inside of MSR zone Z3.

$$v_{S,y}^{Z3} = v_{S,y}^{surf,Z3} + \left(\frac{v^{pull} - v^{cast}}{x_2 - x_1}\right)y^{surf,Z3} - \left(\frac{v^{pull} - v^{cast}}{x_2 - x_1}\right)y \qquad [48]$$

$$v_{S,y}^{Z3} = v_{S,y}^{surf,Z3} + \left(\frac{v^{pull} - v^{cast}}{x_2 - x_1}\right)(y^{surf,Z3} - y) \qquad [49]$$
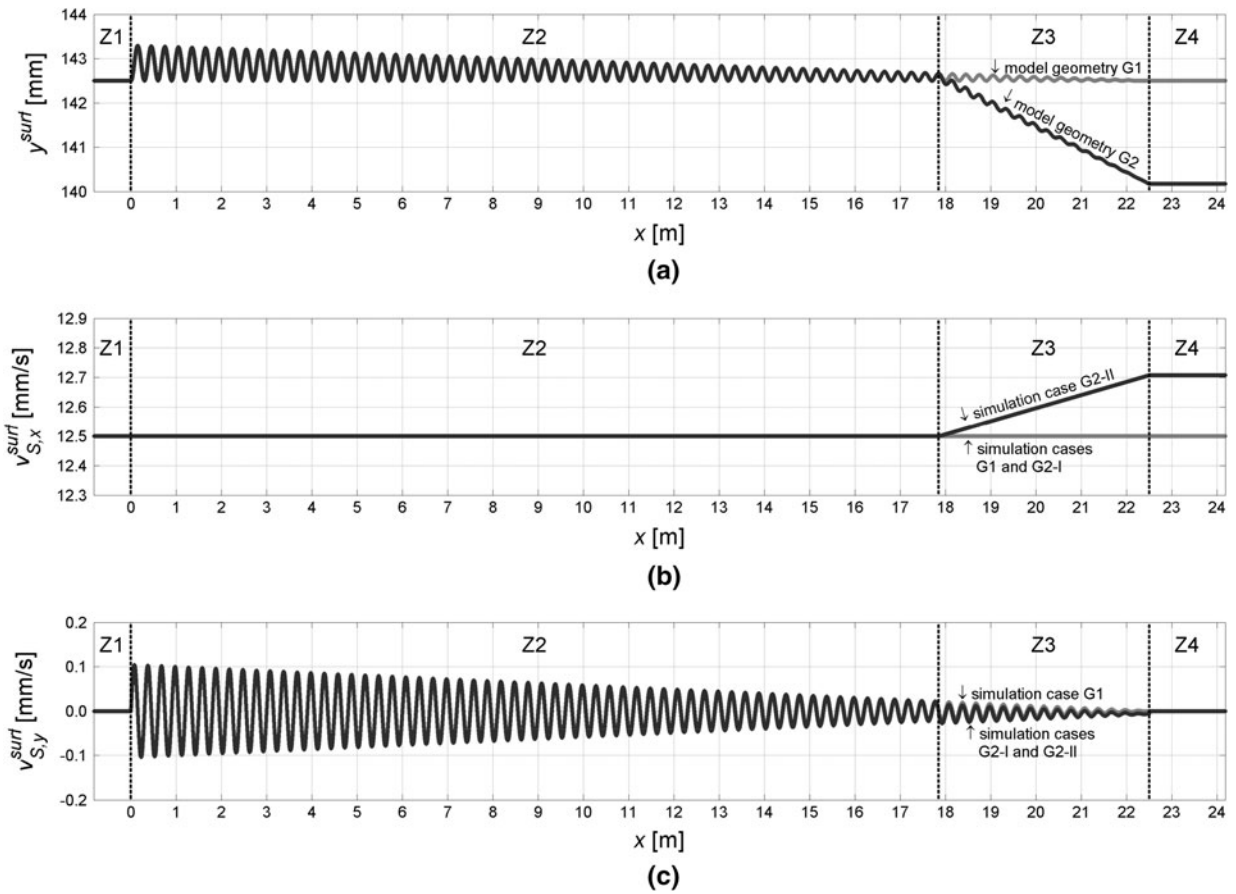
Fig. 2—Contour (*a*) and solid phase velocities in *x*-direction (*b*) and *y*-direction (*c*) at the surface of strand geometries G1 and G2. The dark gray lines show the contour of geometry G2, whereas the light gray lines indicate the different contour of geometry G1 in zones Z3 and Z4.

Notice that the definition of the solid velocity component $v_{S,y}$ according to Eq. [49] is appropriate, as long as the dendrites do not meet at the centerline of the strand. With advancing solidification the growing dendrites reach the center and the dendrite tips of both strand halves touch each other. Hence, the touching tips are locally deformed due to the motion of the solid strand shell. Since bulging appears in zones Z2 and Z3, two sub-domains (A and B) are distinguished between f_S^{zero} and $f_S = 0$ to consider tip deformation. A and B are schematically illustrated in Figure 3. In Eqs. [50] and [51], $v_{S,y}^{zero}$ represents the solid phase velocity in *y*-direction occurring at the position where $f_S = f_S^{zero}$.

- Sub-domain A ($v_{S,y}^{zero} > 0$): This domain is located behind each guiding roll. Since the strand widens behind the rolls, the dendrites move away from the strand center inside of domain A. The *y*-component of the inner solid velocity, $v_{S,y}^A$, is equal to the velocity $v_{S,y}^{zero}$ at the solid fraction f_S^{zero}. Therefore,

$$v_{S,y}^{A,Z2-Z3} = v_{S,y}^{zero,Z2-Z3}. \quad [50]$$

- Sub-domain B ($v_{S,y}^{zero} < 0$): This domain is located in front of each guiding roll where the solid is forced

to move toward the strand center. Hence, the previously described deformation of the dendrites between f_S^{zero} and $f_S = 0$ occurs. Inside of domain B, the *y*-component of the solid velocity, $v_{S,y}^B$, is assumed to decrease exponentially from the zero-strength velocity $v_{S,y}^{zero}$ at f_S^{zero}:

$$v_{S,y}^{B,Z2-Z3} = v_{S,y}^{zero,Z2-Z3} \left(1 - \exp\left(a\frac{(f_S^{cent} - f_S)}{(f_S^{zero} - f_S)^b}\right)\right). \quad [51]$$

Although the function of Eq. [51] is a rough assumption, recent investigations show its qualitative suitability to approximate the deformation velocity for macrosegregation simulations.[26,27]

D. *Mesh, Boundary Conditions, and Material Data*

Using the software GAMBIT, a regular 2D finite volume mesh with 145,000 elements and about 150,000 nodes (approximate element size 5 × 5 mm) is assigned to the model geometry representing a cast strand of $l = 25,000$ mm and $w/2 = 142.5$ mm.

Directly at the strand center (boundary "A") a symmetry condition is applied. The environment of the
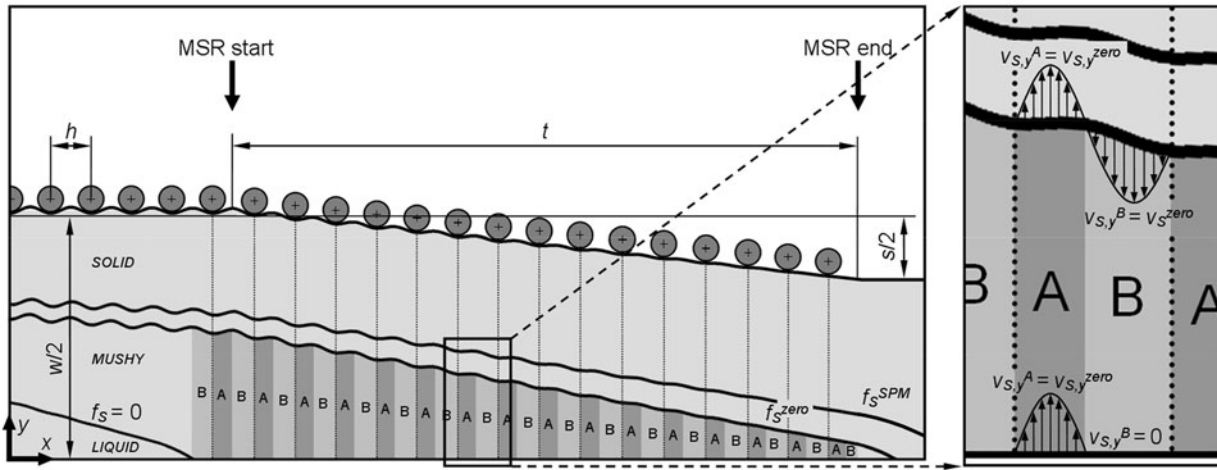
Fig. 3—Location of sub-domains A and B inside of the mushy zone with the corresponding solid phase velocities, schematically shown for model geometry G2. In sub-domain A the dendrites move away from the strand center because the strand widens, whereas in sub-domain B the mushy zone is compressed. The described mushy zone movement occurs periodically at each guiding roll.
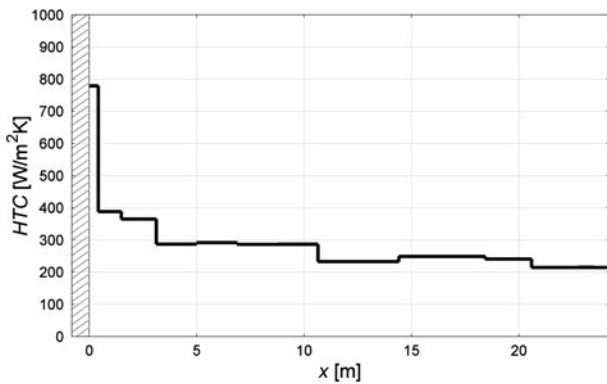
Fig. 4—Heat transfer coefficient (HTC) at the surface of the cast strand. Instead of the HTC, a constant heat flux of 880 kW m^{-2} was predefined at the mold zone for $x < 0$.
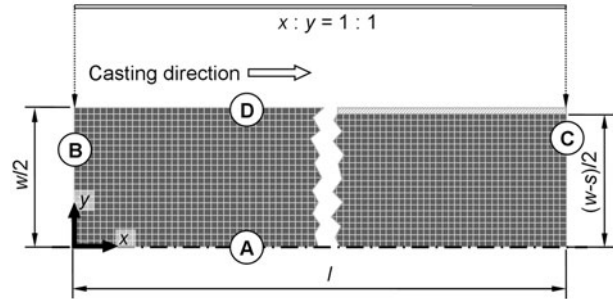
Fig. 5—Marginal areas of the meshed 2D model geometry and location of different boundary conditions "A" to "D". The hatched area at boundary "D" indicates the thickness difference due to MSR between model geometries G1 and G2. The original length-to-thickness ratio (x:y = 1:1) of the mesh is shown by the thin rectangle above.

strand is assumed to have constant temperature T^{envi} and constant atmospheric pressure p^{envi}. A pressure boundary condition is applied at the inlet of the simulation domain (boundary "B" at $x = x_{-1}$) to consider that p^{envi} acts on the melt pool in the mold. The melt entering the domain through the inlet has the initial carbon concentration $C_{L,0}^{C}$, the initial liquid fraction $f_{L,0}$ and the casting temperature T^{cast}. At the outlet of the simulation domain (boundary "C" at $x = x_3$), the velocity boundary condition $v_{S,x} = v^{cast}$ is considered for simulation cases G1 and G2-I. However, for simulation case G2-II $v_{S,x} = v^{pull}$ at the outlet. A heat transfer coefficient (HTC) is assigned to those boundaries of the model, which represent the strand surface (boundary "D"). According to industrial investigations at voestalpine Stahl GmbH this HTC shows a distinct variation along the strand length, as shown in Figure 4.[28] The mesh and the position of the different

Table III. Boundary Conditions and Empirical Parameters

Casting Velocity	v^{cast}	700 to 735 mm min^{-1}
Casting Temperature	T^{cast}	1833 K (1560 °C)
Environment Temperature	T^{envi}	309 K (36 °C)
Atmospheric Pressure	p^{envi}	101,325 Pa
Initial Carbon Concentration	$C_{L,0}^{C}$	0.182 wt pct
Initial Liquid Fraction	$f_{L,0}$	0.99999
SPM Starting Solid Fraction	f_{S}^{SPM}	0.95
Zero-Strength Solid Fraction	f_{S}^{zero}	0.80
Empirical Constant	a	50
Empirical Constant	b	0.25

boundary conditions "A" to "D" are shown schematically in Figure 5, the specific data to describe these boundaries are summarized in Table III.

An overview about the thermophysical and thermodynamic material data used in the simulations is given in Table IV.

Density of the Liquid Phase	ρ_L	7027 kg m^{-3}
Density of the Solid Phase	ρ_S	7324 kg m^{-3}
Specific Heat Capacity (Liquid)	$c_{p,L}$	808.25 J kg^{-1} K^{-1}
Specific Heat Capacity (Solid)	$c_{p,S}$	808.25 J kg^{-1} K^{-1}
Thermal Conductivity (liquid)	k_L	29 W m^{-1} K^{-1}
Thermal Conductivity (Solid)	k_S	35 W m^{-1} K^{-1}
Dynamic Viscosity (Liquid)	η_L	0.0056 kg m^{-1} s^{-1}
Diffusion Coefficient (Liquid)	D_L	2×10^{-8} m^2 s^{-1}
Eutectic Carbon Concentration	γ	4.3 wt pct
Liquidus Slope	m	-116.7 K wt pct^{-1}
Partition Coefficient	k	0.36
Melting Temperature of Pure Fe	T_m^{Fe}	1811 K
Latent Heat	ΔH_m	2.8×10^5 J kg^{-1}
Primary Dendrite Arm Spacing	λ_1	1 mm

III. RESULTS

A. Temperature, Solid Fraction, and Macrosegregation Patterns

As an example, Figure 6(a) shows the typical temperature distribution inside of the strand for simulation case G2-II. With an initial temperature of $T^{cast} = $ 1833 K (1560 °C), the melt enters the strand through the boundary at the left. Because rapid cooling is applied at the upper boundary, the temperature decreases immediately at the strand surface, whereas the center still contains hot melt at its initial temperature. Depending on the declining temperature in the outer strand regions, solidification starts and the solid strand shell grows. Hence, the solid volume fraction increases from the strand's center toward its surface. In Figure 6(b), the crater-shaped solid fraction pattern inside of the strand, which is typical for steel continuous casting, is depicted. Obviously, the temperature distribution of Figure 6(a) is directly related to the solid fraction pattern of Figure 6(b).

Nevertheless, the quantity of most interest is the macrosegregation forming during the solidification process inside of the strand. To characterize macrosegregation, the mixture concentration C_M^C is defined for the alloying element carbon, as given in Eq. [52]. Since the presented solidification model is based on the volume-averaging method, the carbon concentrations C_S^C and C_L^C of the solid and the liquid phase must be considered:

$$C_M^C = \frac{f_L \rho_L C_L^C + f_S \rho_S C_S^C}{f_L \rho_L + f_S \rho_S}. \qquad [52]$$

Figure 6(c) shows the obtained macrosegregation pattern for simulation case G2-II. Since this pattern looks very similar for all of the three simulation cases at first sight, it is necessary to examine and to compare the segregations in detail at selected positions. These positions, which are marked with white dashed lines in Figure 6(c), are:

- pos. 1: the fully solid cross-section at the end of the modeled strand
- pos. 2: the strand centerline
- pos. 3: a straight path at the distance of 10 mm parallel to the centerline.

B. Macrosegregation Profiles

In the current model, the strand geometry and therefore the mesh are predefined analytically for each simulation case, because no thermo-mechanical deformation of the solid strand shell is calculated. Hence, the bulging height at a particular strand position x does not depend on the actual thickness of the solidified shell. This fact is important for understanding the general tendency of the macrosegregation profiles depicted in this section, where positive macrosegregation declines with increasing casting speed. The higher the casting speed v^{cast}, the longer is the liquid core (or the so-called "metallurgical length") at the center of the cast strand. As an example, Figure 7 shows the influence of two different casting velocities on the metallurgical length for model geometry G1. At low casting speeds (Figure 7(a)), the bulging influence on the macrosegregation formation is reinforced, because bulging acts close to the zone of final solidification where the melt is highly enriched with segregated alloying elements. However, at higher casting speeds (Figure 7(b)) the metallurgical length increases and bulging does not act directly at the zone of final solidification, because the strand surface is already flat there.

1. Cross-section macrosegregation profiles (pos. 1)

At $x = x_3 = 24.18$ m, the entire cross-section of the strand is totally solid ($f_S \geq 0.95$). Hence, it is not possible to modify the macrosegregation thereafter. Figure 8 shows the macrosegregation profiles along the thickness direction of the modeled strand half for simulation cases G1, G2-I, and G2-II. In industrial casting processes, the desired cross-section profile would be a straight vertical line indicating no segregations inside of the strand. However, as shown in Figures 8(a) through (c), the most distinct differences to such a perfect homogeneous alloying element distribution occur in the region close to the strand center. The typical macrosegregation profiles being observed in continuous steel casting have a strongly positive peak directly at the strand center which is accompanied with a negative segregation valley beside. Comparing these segregation profiles for a certain casting speed indicates that the maximum and minimum values differ distinctly in the three simulation cases. To investigate the reason for that, the macrosegregation evolution directly at the strand's centerline (pos. 2) and at the distance of 10 mm parallel to the centerline (pos. 3) is described in detail hereafter.

2. Centerline macrosegregation profiles (pos. 2)

For simulation cases G1, G2-I, and G2-II, the obtained macrosegregation as well as the corresponding solid fraction profiles along the strand center are illustrated in Figure 9. It is obvious that centerline macrosegregation formation is related to the appearance of the solid phase at the strand center. For each simulation case, first centerline segregation forms, when the solidification front reaches the center at $x \approx 16.0$ m and the solid fraction starts to rise there. At $x = x_3 = 24.18$ m, the appearing segregation does not
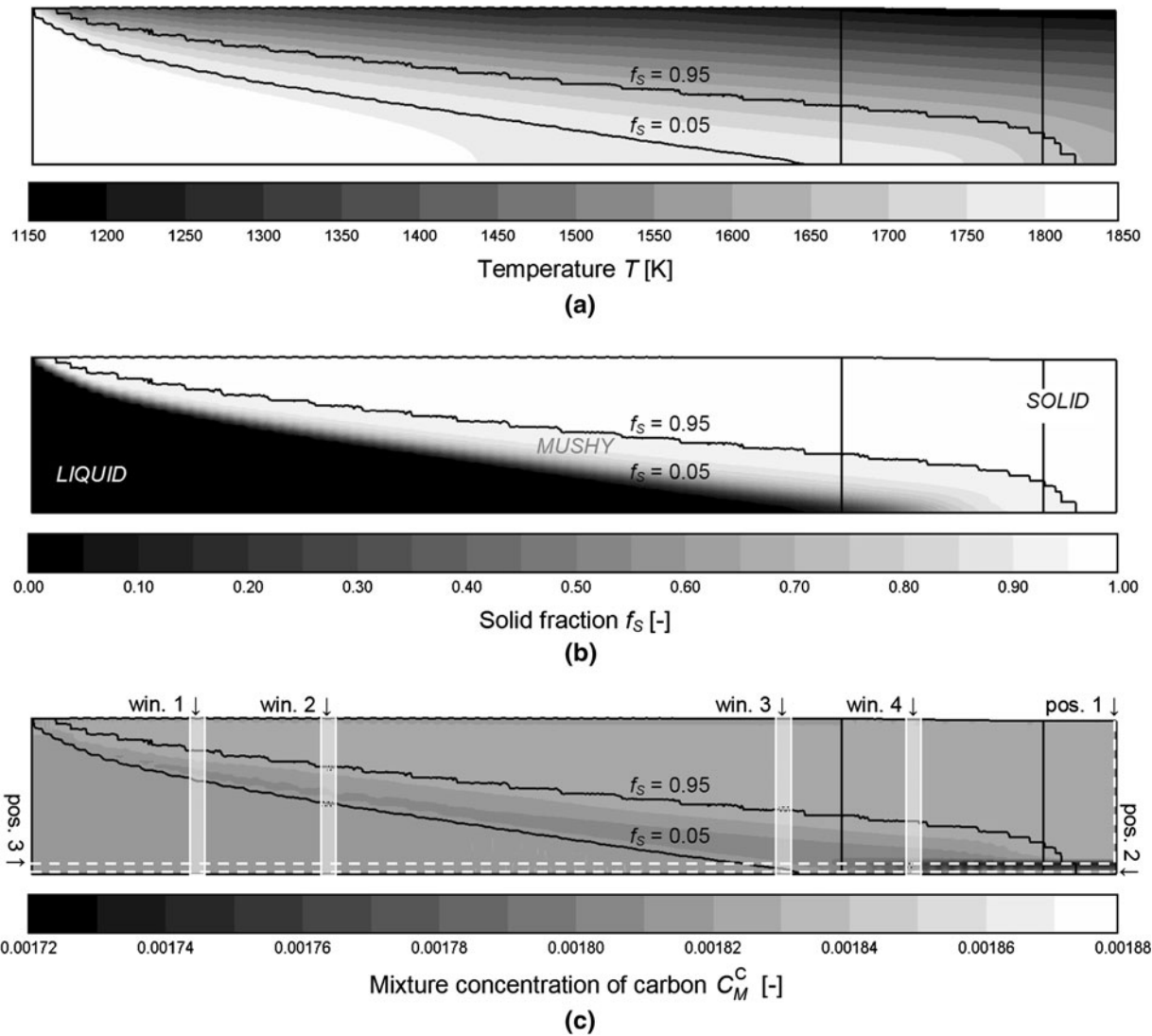
Fig. 6—Temperature (*a*), solid fraction (*b*), and macrosegregation (*c*) patterns inside the upper strand half for simulation case G2-II. For proper visualization, a length scaling of $x{:}y = 1{:}25$ is applied.

change any more, since the solid fraction has already reached the specified limit of total solidification ($f_S \geq 0.95$, dashed horizontal line). Hence, this macrosegregation can be found inside the slabs which are cut off from the fully solidified cast strand.

(a) Simulation case G1 (bulging at constant casting speed): Closer examination reveals that the macrosegregation profiles slightly decrease in periodic waves until they reach a minimum. For example, $v^{cast} = 735$ mm min^{-1} results in a negative segregation of $C_M^C \approx 0.180$ wt pct at $x \approx 20.1$ m. Then the depicted segregation profiles increase until the maximum positive values of C_M^C are reached. This typical segregation behavior in strand casting, based on the relative motion between solid and liquid inside the strand, is due to the combined effects of shrinkage feeding and periodic surface

bulging. On the one hand, feeding causes negative centerline macrosegregation, because the positive segregated melt sucked away from the center flows toward the solidifying strand shell. On the other hand, bulging generates positive macrosegregation caused by a wavy periodic flow at the strand center. When the strand widens behind a guiding roll, enriched melt is sucked toward the centerline. Hence, macrosegregation increases to a local maximum. But when the strand is then compressed at the subsequent roll, the solid is compressed and the liquid is squeezed away from the centerline. Accordingly, macrosegregation decreases to a local minimum. With increasing number of rolls, this macrosegregation waves sum up, as shown in Figure 9(a). The depicted segregation curves base on a competition between both effects: if shrinkage flow dominates, the observed centerline macrosegregation is negative, whereas
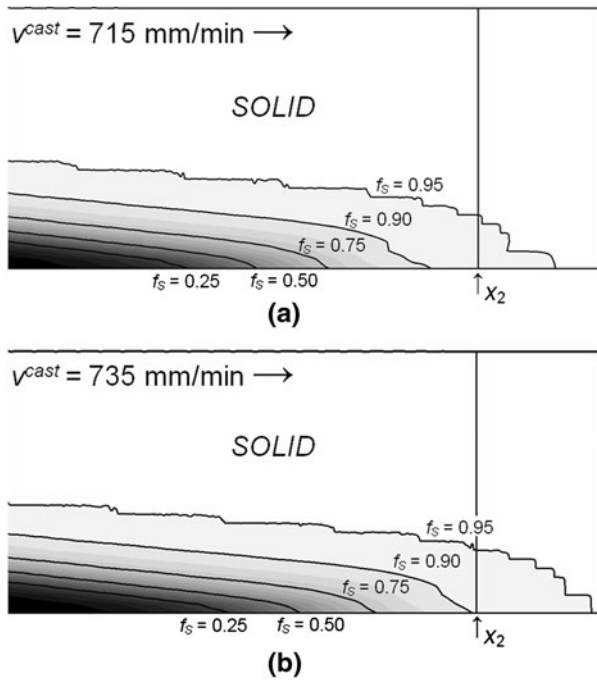
Fig. 7—Influence of different casting velocities on the metallurgical length, shown for simulation case G1; (a) $v^{cast} = 715$ mm min^{-1}, (b) $v^{cast} = 735$ mm min^{-1}. The bulging end position at $x = x_2$ is marked with a vertical black line. For proper visualization, a length scaling of $x{:}y = 1{:}25$ is applied.

positive macrosegregation occurs, if the bulging effect dominates.[17,18]

(b) Simulation case G2-I (bulging and MSR at constant casting speed): Figure 9(b) shows the obtained macrosegregation profiles, if MSR is applied and the casting velocity is treated to be constant at each strand position. Then, an additional phenomenon influences the forming segregation: the cross-section reduction of the strand. Macrosegregation starts to rise, when solidification reaches the strand center at $x \approx 16.0$ m. With slight oscillations caused by strand surface bulging, C_M^C increases rapidly to a positive maximum value at $x \approx 21.2$ m. Thereafter, the segregation profile declines until the end of the MSR zone at $x = x_2 = 22.5$ m is reached. For $x > 22.5$ m, the segregation stays relatively constant. At first sight, MSR does not have the desired reduction effect on the observed centerline segregation. Quite the contrary happens, if MSR is applied: comparing the curves in Figures 9(a) and (b) for identical casting speeds implies higher instead of lower segregations at the strand end. Due to the cross-section reduction in the MSR zone, the already solidified strand shell is forced toward the strand center where the melt is displaced by the solid. Thus, the metallurgical length decreases although the casting speed does not change. Since the bulging end position is fixed in the current model, bulging acts at an area of higher segregated melt which enhances the formation
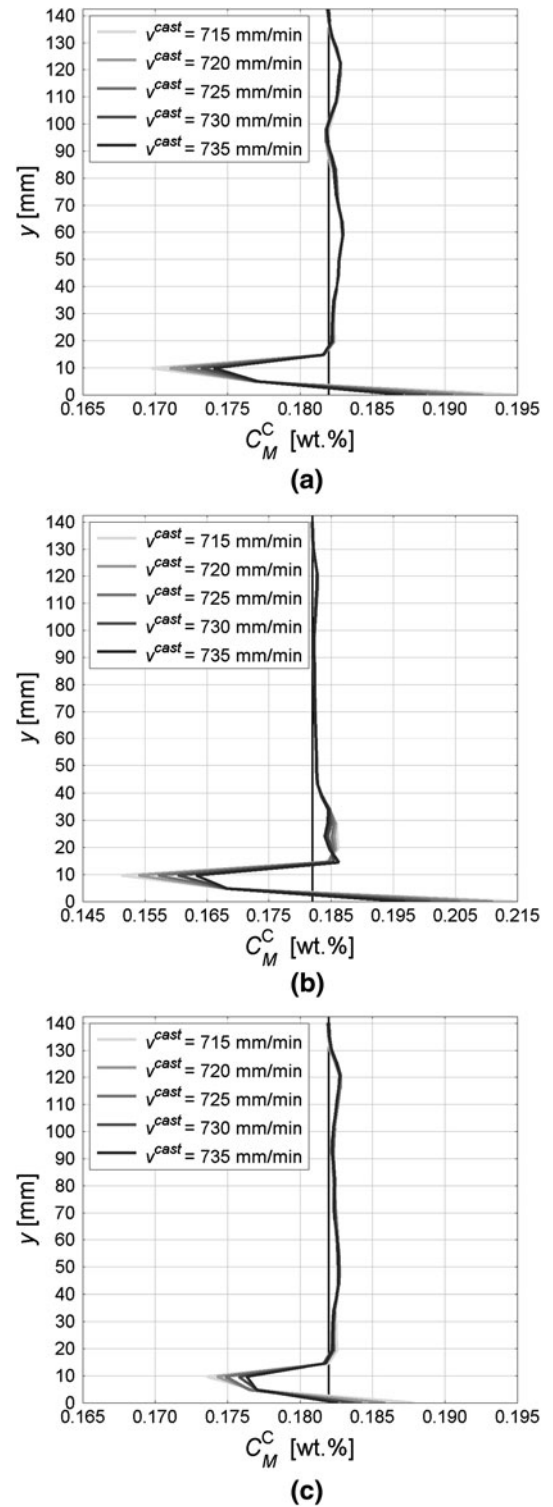
Fig. 8—Macrosegregation profiles depending on different casting velocities along the cross-section of the solidified strand for simulation cases G1 (a), G2-I (b), and G2-II (c).

of positive macrosegregation, as already explained. However, focussing on identical metallurgical lengths is a precondition for comparing the different simulation cases in the current simulation model.
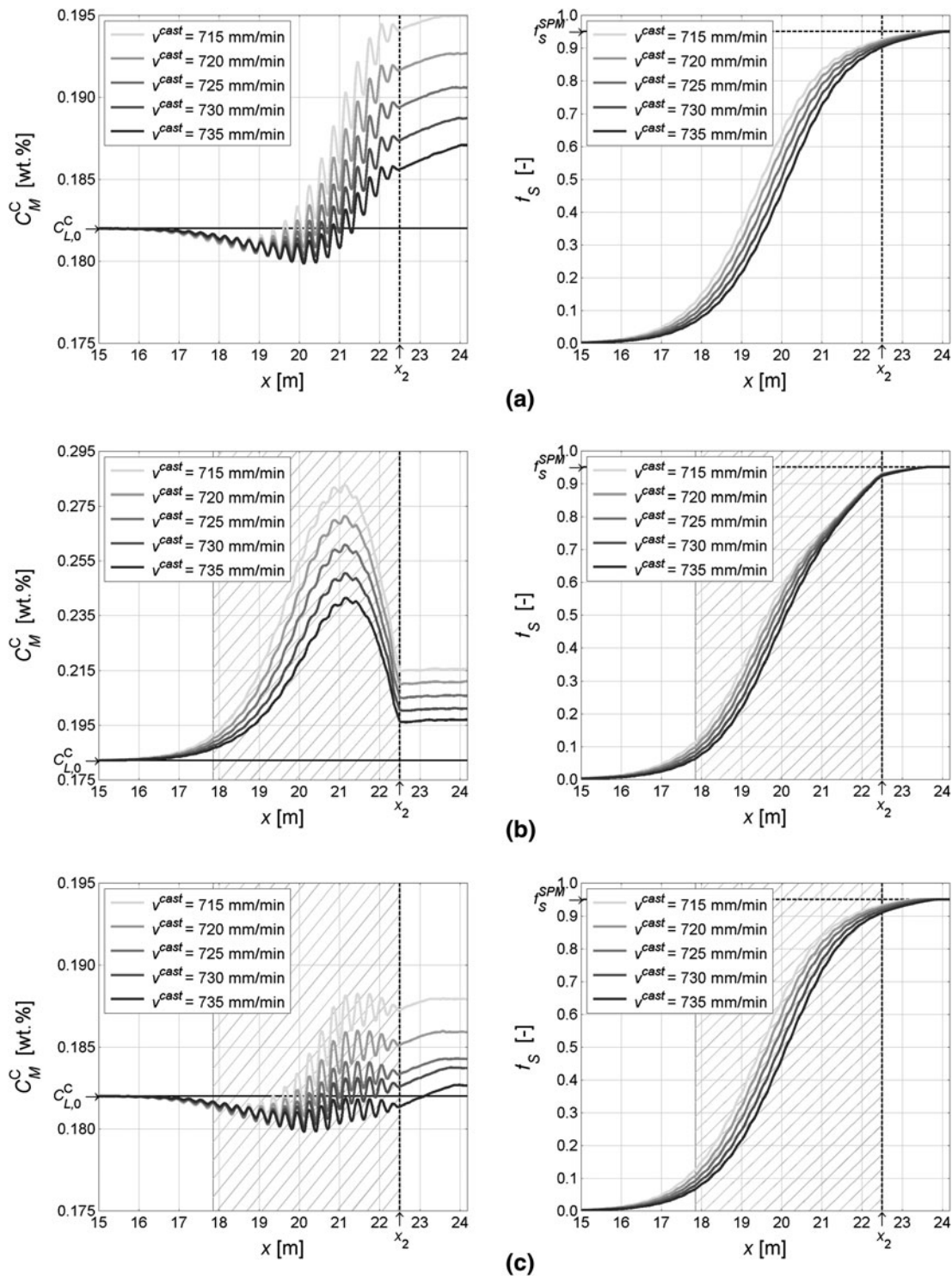
Fig. 9—Macrosegregation (left column) and solid fraction (right column) profiles along the strand centerline depending on different casting velocities for simulation cases G1 (*a*), G2-I (*b*), and G2-II (*c*). The bulging and MSR end positions at $x = x_2$ are marked with vertical black lines; the hatched areas indicate the position of the MSR zone for the simulation cases which consider MSR.

(c) Simulation case G2-II (bulging and MSR with varying casting speed): The centerline segregation and solid fraction profiles obtained for simulation case G2-II are illustrated in Figure 9(c). They look qualitatively similar to the profiles of case G1 shown in Figure 9(a). Although the solid fraction profiles obtained in both simulation cases are practically identical, the macrosegregation achieved with MSR in case G2-II is lower than the segregation achieved without MSR in case G1. At $x = x_3 = 24.18$ m for example, macrosegregation decreases from $C_M^C = 0.195$ wt pct to $C_M^C = 0.188$ wt pct at a casting
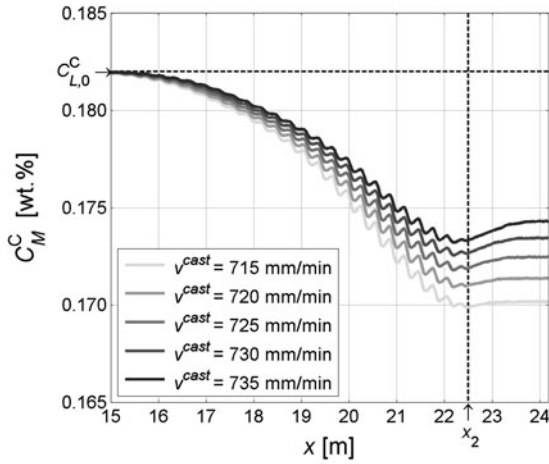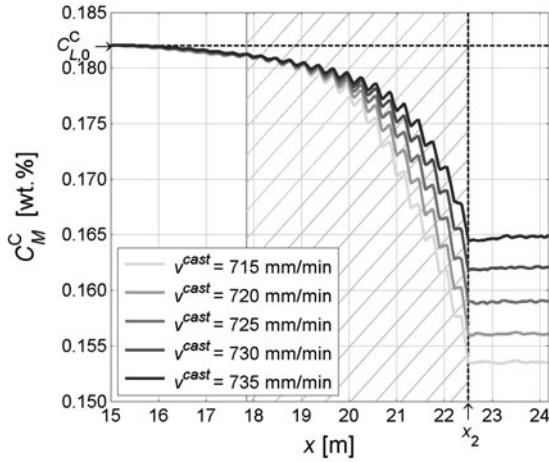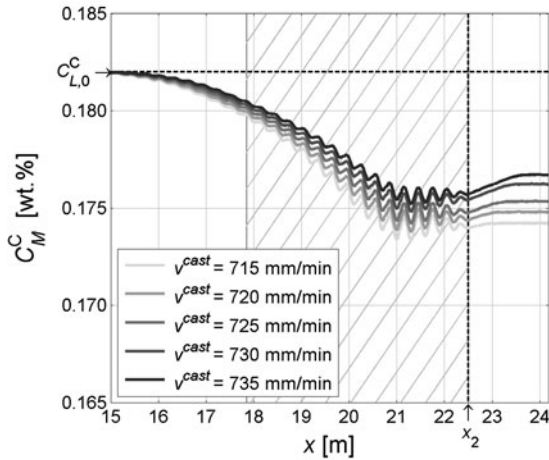
Fig. 10—Macrosegregation profiles at the distance of 10 mm parallel to the strand center depending on different casting velocities for simulation cases G1 (*a*), G2-I (*b*), and G2-II (*c*). The bulging and MSR end position at $x = x_2$ is marked with a vertical black line; the hatched areas indicate the position of the MSR zone.

speed of 715 mm min^{-1}. Obviously, this simulation case shows the expected effect of reducing centerline macrosegregation.

3. Close-to-centerline macrosegregation profiles (pos. 3)

For each of the three simulation cases, positive macrosegregation can be found directly at the strand centerline. However, only a few millimeters beside the situation is completely different. As shown in Figure 10, only negative segregation appears at the distance of 10 mm parallel to the center.

IV. DISCUSSION

A. *Influence Factors on Macrosegregation Formation*

A mathematical relationship is given in Eq. [53] to analyze the different influence factors on macrosegregation formation and to support the interpretation and the understanding of the obtained simulation results. To derive Eq. [53] as set out in the Appendix, steady-state conditions ($\partial/\partial t = 0$), different densities for the liquid and the solid phase ($\rho_L \neq \rho_S$) as well as the non-divergence-free deformation of the solid ($\nabla \cdot \vec{v}_S \neq 0$) are considered:

$$\nabla \tilde{C}_M \cdot \vec{v}_S = f_S \rho_S (C_L - C_S) \nabla \cdot \vec{v}_S + \vec{v}_S C_L (\rho_S - \rho_L) \cdot \nabla f_S - f_L \rho_L (\vec{v}_L - \vec{v}_S) \cdot \nabla C_L. \qquad [53]$$

Notice that the differences $C_L - C_S$ and $\rho_S - \rho_L$ are positive for practically relevant solidification problems. For understanding of the mechanisms described with Eq. [53], the Lagrangian formulation of the following two quantities is quite useful:

$$\nabla \tilde{C}_M \cdot \vec{v}_S = \frac{d\tilde{C}_M}{dt} \quad \text{and} \quad \nabla f_S \cdot \vec{v}_S = \frac{df_S}{dt}. \qquad [54]$$

In Eq. [54], the change of the volume specific mixture concentration with time, $d\tilde{C}_M/dt$, quantifies macrosegregation formation, whereas the time-dependent change of the solid fraction, df_S/dt, represents solidification inside of the moving cast strand. Since the change of $\tilde{C}_M$ depends on a competition between the three terms at the right-hand side of Eq. [53], the final macrosegregation that can be found at a certain position inside of the continuous casting strand is related to the contribution of the most dominant term.

1. *Solid phase deformation*

Solid phase deformation is quantified by the divergence of the solid velocity, $\nabla \cdot \vec{v}_S$. Compression due to bulging and/or softreduction ($\nabla \cdot \vec{v}_S$ is negative) results in an accumulation of the solid being less segregated than the melt, which reduces $\tilde{C}_M$. However, $\nabla \cdot \vec{v}_S$ can also take positive values, if the strand widens behind a guiding roll and the dendrites move away from the strand center. That enhances the formation of positive macrosegregation particularly at the strand centerline. With increasing concentration difference $C_L - C_S$ the contribution of the deformation term of Eq. [53] is reinforced. Notice that solid deformation itself affects macrosegregation formation, but deformation also

induces relative motion between the phases which can be the reason for segregation formation as well.

2. *Solidification*

The increase of the solid fraction during the casting process is characterized by $\nabla f_S \cdot \vec{v}_S$. Because of $\rho_S > \rho_L$, the volume of the forming solid is smaller than the volume of the liquid. To avoid pore formation, this volume difference due to shrinkage must be compensated by additional melt of concentration C_L. For practically relevant solidification problems, $C_L > C_S$ and $\rho_S > \rho_L$. Therefore, the second term of Eq. [53] can be reasonably presupposed as positive for such problems. Hence, $\tilde{C}_M$ increases because the formation of positive macrosegregation is enhanced. The higher the density difference $\rho_S - \rho_L$ between the solid and the liquid, the stronger is the contribution of the solidification term. Notice that solidification causes macrosegregation formation which is related to the density difference between the phases. Furthermore, flow to compensate the volume shrinkage occurs when the melt is sucked into the solidifying regions. This relative motion due to shrinkage feeding flow also influences macrosegregation formation.

3. *Relative velocity*

As previously discussed, solid phase deformation and solidification lead to the formation of macrosegregation. However, both of these effects induce additional relative velocities between the liquid and the solid, which are expressed by $\vec{v}_L - \vec{v}_S$. If the scalar product between the relative velocity vector and the gradient of the liquid phase concentration, ∇C_L, is positive (*e.g.*, if both vectors are orientated into the same direction), the third term of Eq. [53] is negative. Hence, $\tilde{C}_M$ decreases because macrosegregation formation is reduced. By contrast, if the scalar product is negative (*e.g.*, the relative velocity vector and the concentration gradient have reverse orientations), the third term of Eq. [53] is positive. That means macrosegregation formation is enhanced. Since the relative velocity is identified as key factor to influence macrosegregation formation, a detailed examination of the melt flow patterns near the strand center is advisable to analyze segregation formation in detail.

B. *Melt Flow Patterns*

Examining the relative motion between the solid and the liquid phase provides a valuable contribution for understanding segregation formation. Thus, the melt flow patterns (relative velocity patters) are visualized in Figure 11 for the simulation cases G1, G2-I, and G2-II at four distinct strand positions. Each position is marked with a rectangular "window" in Figure 6(c):

- win. 1: at guiding roll 10 ($x = 3.0$ m) inside the first half of the secondary cooling zone
- win. 2: at guiding roll 20 ($x = 6.0$ m) inside the first half of the secondary cooling zone
- win. 3: at guiding roll 55 ($x = 16.5$ m) directly in front of the MSR zone
- win. 4: at guiding roll 65 ($x = 19.5$ m) inside the MSR zone

As shown in Figure 11, three regions exist inside the strand: the solid strand shell, the liquid strand core and the two-phase mushy zone in between. The solid region is delimited by f_S^{SPM}. Beyond this volume fraction solidification has already finished and therefore no relative motion occurs. With increasing strand coordinate or roll number, respectively, the thickness of the solid region grows and the liquid region at the strand center gets thinner.

1. *Flow pattern at roll 10 (win. 1)*

At guiding roll 10, the typical relative melt flow pattern caused by strand shell bulging can be observed. In front of the roll the solid shell is forced to move toward the strand center, whereas the shell moves away from the center when the strand widens up behind the roll. The relative melt flow is orientated against the movement direction of the solid shell resulting in a wavy flow pattern. In Figure 11, the waves are clearly visible for simulation case G2-I, because there the relative velocity component in *x*-direction is smaller than in the other two cases. Hence, the component in *y*-direction has a stronger impact on the orientation of the depicted velocity arrows. Inside the mushy zone, the melt is sucked into the solidifying regions to compensate the shrinking volume of the solid phase. Volume shrinkage occurs, because the solid phase has a higher density than the melt. As indicated by the grayscale in Figure 11, the magnitude of the relative velocity is about 1,000 times smaller inside the mushy zone than in the liquid core region.

2. *Flow pattern at roll 20 (win. 2)*

At the position of guiding roll 20, the unidirectional relative flow in the cast direction is still apparent for simulation cases G1 and G2-II; the depicted flow patterns look similar to those at roll 10. However, for case G2-I the pattern is completely different, because distinct flow vortexes occur at the positions of the local bulging maxima in front as well as behind roll 20. As shown in Figure 11, these vortexes emerge only at the fully liquid core region, whereas the feeding flow direction deep inside the mushy zone is not affected. In principle, vortex flow would have a favorable effect on the macrosegregation formation, since the segregated melt is transported away from the solidification front and mixed with unsegregated melt from the central core region. Unfortunately, this phenomenon is limited to a short strand section. To find the reason for the vortex formation, one has to examine a different strand position some meters apart, namely close to the MSR zone.

3. *Flow pattern at roll 55 (win. 3)*

At guiding roll 55, only a thin liquid channel remains at the strand center. As shown in Figure 11, the relative melt flow inside this channel is orientated in the cast direction for simulation cases G1 and G2-II. However, the velocity arrows point into the opposite direction for
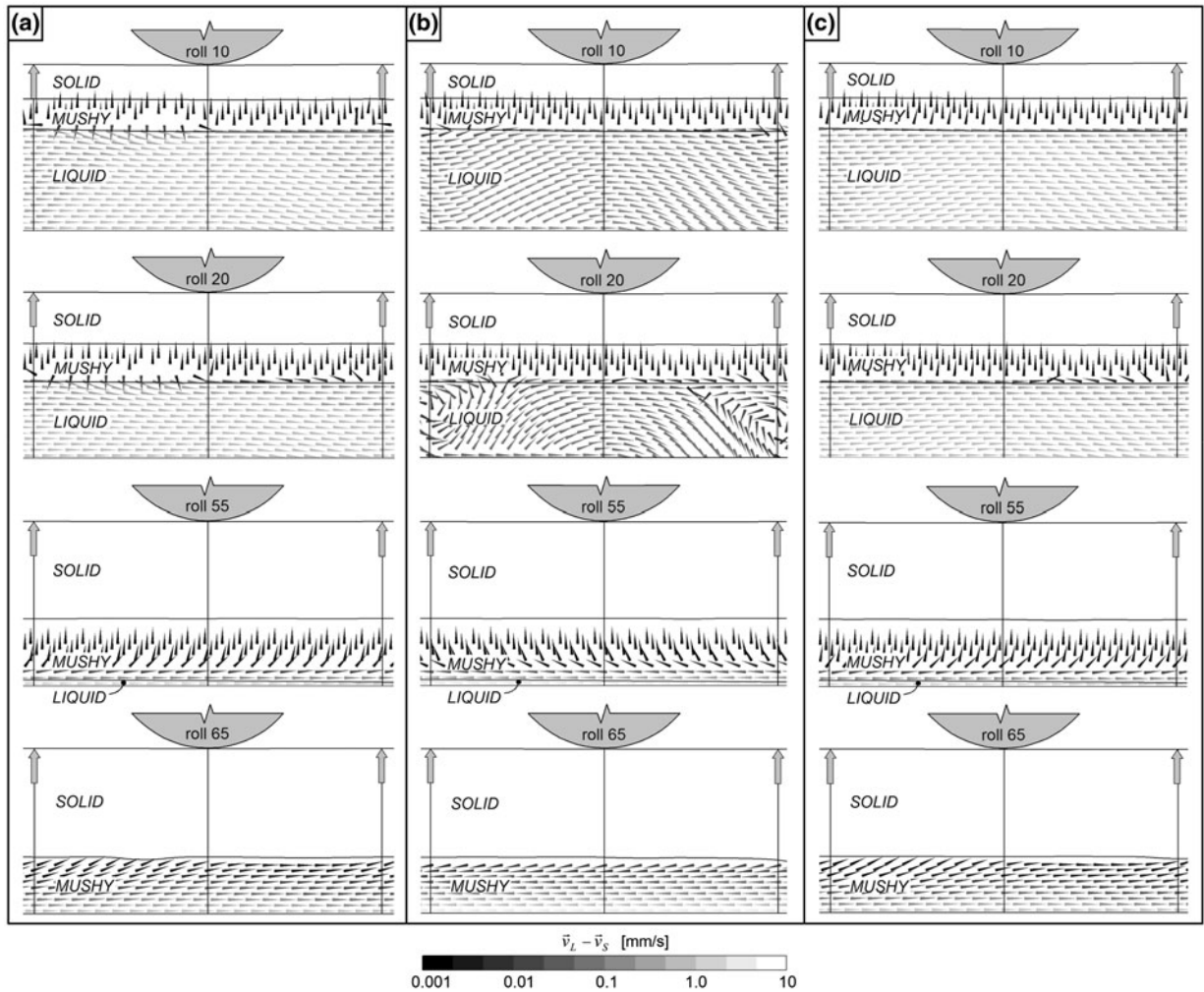
Fig. 11—Patterns of relative melt flow for simulation cases G1 (*a*), G2-I (*b*), and G2-II (*c*) at 4 different strand positions: at roll 10 ($x = 3.0$ m), at roll 20 ($x = 6.0$ m), at roll 55 ($x = 16.5$ m), and at roll 65 ($x = 19.5$ m). The casting velocity is 715 mm min^{-1}. All arrows have uniform length to visualize also slow melt motions. The local melt flow direction is indicated by the arrow orientation, whereas the logarithmic gray scale quantifies the velocity magnitude. The two vertical arrows beside the schematically drawn guiding roll indicate the positions of the local bulging maxima.

case G2-I. Comparatively high relative velocities ($\vec{v}_L - \vec{v}_S > 1$ mm s^{-1}) occur inside the channel, which explains why vortexes must form for case G2-I somewhere inside the strand: the melt flow coming from the casting mold on the left meets the relative flow coming from the strand end region on the right. In all of the three simulation cases feeding flow still exists, but the required liquid is sucked from different strand regions. Particularly in case G2-I, feeding is achieved with the highly segregated melt from the solidification crater tip. That results in an additional distinct positive macrosegregation peak between $y \approx 15$ mm and $y \approx 40$ mm, as shown in Figure 8(b). For comparison, such a segregation peak does not appear for cases G1 and G2-II, which are represented by Figures 8(a) and (c), respectively.

4. *Flow pattern at roll 65 (win. 4)*

At guiding roll 65, which is a part of the MSR segment in simulation cases G2-I and G2-II, the two-phase mushy zone has already reached the strand center.

The segregation profiles depicted previously in Figure 9 indicate that this strand region is crucial for the formation of centerline macrosegregation. Since both phases, solid and liquid, are apparent at the strand center, relative motion between these phases occurs.

As already discussed in Section III–B–2(a), formation of centerline macrosegregation in simulation case G1 is dominated by bulging induced melt flow. When the strand widens due to cyclic surface bulging, segregated melt is sucked toward the center. Hence, macrosegregation locally increases according to the third term of Eq. [53]. In contrast, when the strand is compressed, the melt is pushed away from the center and the dendrites are deformed there. Since the contribution of the third term of Eq. [53] decreases and the influence of the first term on macrosegregation formation increases, centerline segregation is locally reduced. To analyze the MSR effect in simulation cases G2-I and G2-II, the centerline segregation and the flow pattern of simulation case G1 are taken as reference.

In simulation cases G2-I and G2-II, the observed relative melt flow at the strand center in or against the cast direction, respectively, depends on the velocity definition. If the solid phase velocity is related to the actual strand cross-section (*e.g.*, $v_{S,x}$ increases with decreasing cross-section area, case G2-II) the relative velocity vectors are oriented in the cast direction. This flow pattern looks similar to the pattern of case G1 without MSR. However, due to the cross-section reduction the dendrites at the strand center are additionally compressed in case G2-II. As given by the first term of Eq. [53], solid phase compression decreases macrosegregation. Therefore, the macrosegregation profiles in Figure 9(c) are qualitatively similar to the profiles in Figure 9(a), but the finally achieved macrosegregation is lower.

In contrast, if the solid phase moves with constant $v_{S,x}$, the volume of the phases inside the MSR zone must be reduced proportional to the decreasing cross-section to fulfill the continuity law. Since the liquid as well as the solid are incompressible and the solid movement is constrained, volume change may only be achieved by displacing the liquid. Accordingly, the melt enriched with carbon is pressed out of the MSR zone. It is forced to flow against the cast direction, and therefore against the concentration gradient inside of the liquid phase. As given in Eq. [53], this kind of flow pattern supports the formation of positive centerline segregation, because the relative velocity vectors and the concentration gradient have opposite directions. However, the cross-section reduction within the MSR segment leads also to a compression of the solid phase. Due to the non-divergence-free velocity definition of simulation case G2-I, this solid phase deformation occurs within the entire MSR zone. Thus, the first term of Eq. [53] which quantifies the deformation becomes increasingly dominant. According to the varying contributions of both terms, the hill-shaped centerline segregation profiles shown in Figure 9(b) develop: after the profiles increase rapidly between $x \approx 16.0$ m and $x \approx 21.0$ m, they finally decrease between $x \approx 21.0$ m and $x \approx 22.5$ m.

C. Position of the MSR Segment

Table V gives an overview about the centerline solid fractions occurring at the start ($x = x_1$) and at the end ($x = x_2$) position of MSR for simulation cases G2-I and G2-II. For comparison, the table also contains the solid fractions at the same positions for simulation case G1, although MSR is not applied therein.

Figure 12 shows the influence of the centerline solid fraction f_S^{cent} at the start (a) and at the end (b) position of the MSR segment on the centerline segregation C_M^C observed at the fully solid strand end ($x = x_3$). Gener-

Table V. Centerline Solid Fractions at the Start and End Positions of MSR

v^{cast}	G1		G2-I		G2-II	
	f_S^{cent} at x_1	f_S^{cent} at x_2	f_S^{cent} at x_1	f_S^{cent} at x_2	f_S^{cent} at x_1	f_S^{cent} at x_2
715 mm min^{-1}	0.1252	0.9255	0.1136	0.9293	0.1254	0.9326
720 mm min^{-1}	0.1072	0.9211	0.0986	0.9282	0.1073	0.9287
725 mm min^{-1}	0.0916	0.9162	0.0854	0.9273	0.0917	0.9238
730 mm min^{-1}	0.0780	0.9101	0.0729	0.9255	0.0781	0.9171
735 mm min^{-1}	0.0664	0.9030	0.0625	0.9235	0.0665	0.9099
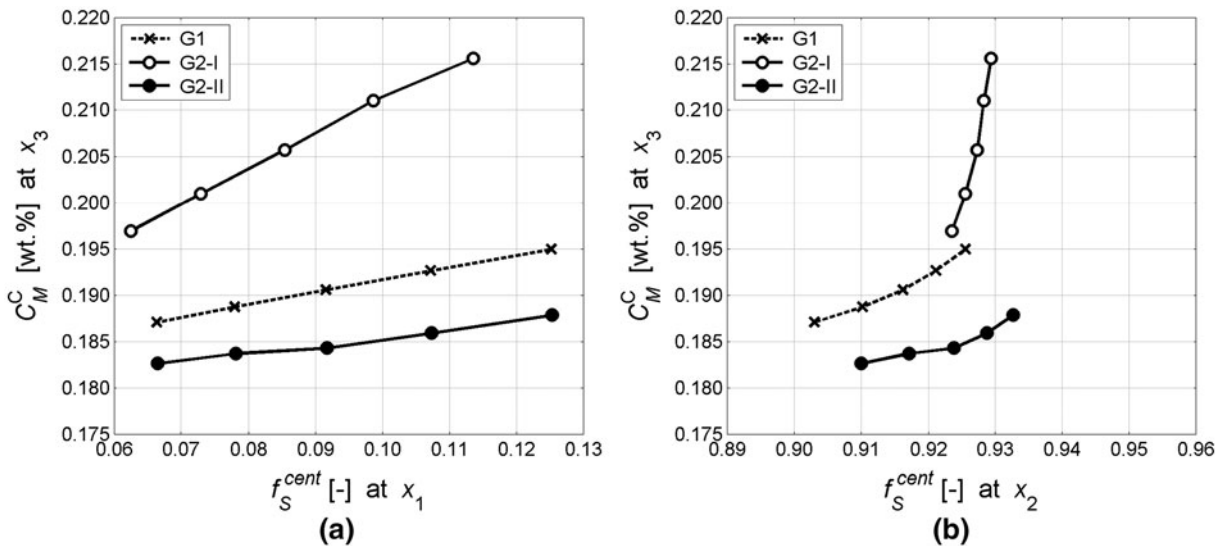
Fig. 12—Centerline macrosegregation at the strand end ($x = x_3$) depending on the centerline solid fraction at the start ($x = x_1$) and at the end ($x = x_2$) position of the MSR segment. The broken line is just plotted for comparison, although no MSR is applied for case G1.

ally, C_M^C increases with increasing f_S^{cent}. However, comparing the slopes of the lines depicted in Figures 12(a) and (b) indicates that f_S^{cent} at the MSR end position x_2 has a stronger impact on the forming segregation than f_S^{cent} at the MSR start position x_1. For all simulation cases, a slightly higher centerline solid fraction f_S^{cent} at position x_2 results in a strongly increasing centerline segregation C_M^C. Hence, strand surface bulging particularly at high centerline solid fractions must be avoided. Since the effect of MSR counteracts to the effect of bulging, to apply MSR as close as possible at the region of final solidification is efficient for reducing positive centerline segregation.

However, this may cause high deformation forces acting on the MSR segment if an almost solid strand is compressed. Furthermore, to detect exactly the position of final solidification inside of the strand is a challenging task, because the position strongly depends on the particular casting process parameters (*e.g.*, cross-section dimensions of the strand, casting speed, steel composition). Therefore, it has to be remarked again that the current model describes the macrosegregation formation in continuous casting of simple carbon alloyed steel. However, industrially produced steel grades contain additional alloying elements (*e.g.*, Mn, Si, Cr, Mo, *etc.*) which influence the solidification behavior and therefore the metallurgical length of the cast strand as well. Accordingly, the effect of the presented MSR configuration on the macrosegregation formation may differ for multi-component steels.

V. CONCLUSIONS

The presented study investigates the effect of MSR on the formation of centerline macrosegregation in continuous slab strand casting. For that purpose, two 25-m long cast strand geometries are compared: one considers only strand surface deformation due to bulging and the other additionally takes into account the cross-section reduction caused by MSR. Since the simulation model does not consider the thermo-mechanical material behavior, the bulged surface of the continuous casting strand and the movement of the solid phase are predefined analytically. Two different solid velocity definitions are considered to analyze the impact of the MSR-induced deformation on the macrosegregation formation. Depending on these definitions, the macrosegregation profiles obtained in the simulations differ distinctly, because different melt flow patterns occur inside the strand.

1. For casting processes at industrial scale the actual movement of the solid strand shell is much more complex than the assumed movement in the presented simulation cases. The actual shell movement has a significant influence on the forming macrosegregation. This influence depends on three principal factors analyzed in the present simulation study: solidification, deformation and relative melt flow. However, the contribution of these three factors varies for different MSR configurations.

2. If all contributions that influence centerline macrosegregation in continuously cast strands are taken into consideration, the often proposed assumption that an ideal MSR configuration compensates the shrinkage feeding flow is wrong. Both, MSR induced flow and feeding flow, reduce positive centerline macrosegregation in strand casting. In contrast, the up-widening of the strand cross-section caused by surface bulging enhances unfavorable positive centerline segregation. The MSR effect is based on compensating the effect of surface bulging, because MSR modifies the relative melt flow pattern occurring inside of the mushy zone directly at the strand center. The interdependence of both effects gives a hint to the often observed phenomenon of increasing macrosegregation although MSR is applied, because relative melt flow due to an unfavorable MSR configuration may also enhance centerline segregation formation.

3. The bulged surface of the continuous casting strand is assumed to be sinusoidally waved. Although industrial observations confirm this analytical estimation, it is actually unknown how the local bulging height correlates exactly with the solid fraction at the strand center. Nevertheless, the simulations show that the macrosegregation formation is strongly influenced by the centerline solid fraction occurring at the end position of surface bulging. The closer bulging acts to the region of final solidification, the higher is the observed macrosegregation at the strand center. Accordingly, to avoid bulging particularly at this region has the best efficiency on segregation prevention. The key question is not at which position MSR should start. Instead of, the appropriate end position of MSR seems to be more important for achieving the desired effect. This position should be as close as possible to the bulging end position to inhibit bulging induced flow of highly segregated melt at the strand center.

4. Inside of the MSR zone, a small variation of the solid velocity in the cast direction has a strong effect on the melt flow pattern and therefore on the macrosegregation profiles. If the solid velocity is assumed as constant, the relative melt flow at the centerline is orientated against the cast direction. However, if the solid velocity is assumed to increase with decreasing cross-section of the strand, the relative melt flow is orientated in the cast direction. This strong influence of the solid velocity on the macrosegregation formation at the centerline of continuously cast strands was also observed in a previous study.[19]

5. Since 2D model geometries are used in the present simulations, all effects which may concern the width of the continuous casting strand (*e.g.*, lateral strand deformation) are not covered. However, 3D effects may have an influence on the actual strand velocity and therefore on the flow and macrosegregation patterns inside of the strand. Particularly, this is of importance for investigating casting formats of

small width-to-thickness ratios (*e.g.*, cast billets). The numerical model used in the current study disregards pore and crack formation inside the strand. Especially a deeper understanding of the crack formation could be of interest, because an unfavorable choice of the MSR operating parameters can cause this casting defect.

6. The performed numerical simulations are focussed on a certain strand geometry and on a given MSR configuration. Since the strand surface profile is not directly related to the casting speed or to the actual metallurgical length, respectively, two general questions requiring further investigations raised:

  (i) What is the limiting centerline solid fraction, beyond which no strand surface bulging occurs? The higher this limit, the higher is the positive centerline macrosegregation expected to form.
  (ii) What is the actual strand velocity in the cast direction particularly inside of the MSR zone? Even small velocity variations may distinctly influence the formation of centerline macrosegregation.

To answer these questions satisfactorily requires the implementation of a thermo-mechanical model, which is an ongoing task.

APPENDIX

The derivation of Eq. [53] is based on the assumption of steady-state conditions ($\partial/\partial t = 0$), different densities for the liquid and the solid ($\rho_L \neq \rho_S$) as well as the non-divergence-free deformation of the solid ($\nabla \cdot \vec{v}_S \neq 0$). For steady-state conditions, combining the species transfer equations [16] and [17] results in

$$\nabla \cdot (f_L \rho_L \vec{v}_L C_L) + \nabla \cdot (f_S \rho_S \vec{v}_S C_S) = 0. \quad [A1]$$

By applying the chain rule to both terms, Eq. [A1] can be modified to

$$\nabla \cdot (f_L \rho_L \vec{v}_L) C_L + f_L \rho_L \vec{v}_L \cdot \nabla C_L + \nabla (f_S \rho_S C_S) \cdot \vec{v}_S \\ + f_S \rho_S C_S \nabla \cdot \vec{v}_S = 0. \quad [A2]$$

The continuity law for two contributing phases is given as

$$\nabla \cdot (f_L \rho_L \vec{v}_L) + \nabla \cdot (f_S \rho_S \vec{v}_S) = 0, \quad [A3]$$

which can be modified by applying the chain rule to

$$\nabla \cdot (f_L \rho_L \vec{v}_L) = -f_S \rho_S \nabla \cdot \vec{v}_S - \rho_S \vec{v}_S \cdot \nabla f_S. \quad [A4]$$

Then, inserting the right-hand side of Eq. [A4] into Eq. [A2] results in

$$-f_S \rho_S C_L \nabla \cdot \vec{v}_S - \rho_S \vec{v}_S C_L \cdot \nabla f_S + f_L \rho_L \vec{v}_L \cdot \nabla C_L \\ + \nabla (f_S \rho_S C_S) \cdot \vec{v}_S + f_S \rho_S C_S \nabla \cdot \vec{v}_S = 0, \quad [A5]$$

which can be simplified to

$$f_S \rho_S (C_S - C_L) \nabla \cdot \vec{v}_S - \rho_S \vec{v}_S C_L \cdot \nabla f_S + f_L \rho_L \vec{v}_L \cdot \nabla C_L \\ + \nabla (f_S \rho_S C_S) \cdot \vec{v}_S = 0. \quad [A6]$$

Based on the definition of the mixture concentration for carbon given in Eq. [52], the volume specific mixture concentration $\tilde{C}_M$ is introduced:

$$\tilde{C}_M = f_L \rho_L C_L + f_S \rho_S C_S. \quad [A7]$$

Multiplying Eq. [A7] with $\nabla(\ldots) \cdot \vec{v}_S$ results in

$$\nabla \tilde{C}_M \cdot \vec{v}_S - \nabla (f_L \rho_L C_L) \cdot \vec{v}_S - \nabla (f_S \rho_S C_S) \cdot \vec{v}_S = 0, \quad [A8]$$

which is then used to extend Eq. [A6] in the following way:

$$f_S \rho_S (C_S - C_L) \nabla \cdot \vec{v}_S - \rho_S \vec{v}_S C_L \cdot \nabla f_S + f_L \rho_L \vec{v}_L \cdot \nabla C_L \\ + \nabla (f_S \rho_S C_S) \cdot \vec{v}_S + \nabla \tilde{C}_M \cdot \vec{v}_S - \nabla (f_L \rho_L C_L) \cdot \vec{v}_S \\ - \nabla (f_S \rho_S C_S) \cdot \vec{v}_S = 0. \quad [A9]$$

One can simplify Eq. [A9] to

$$\nabla \tilde{C}_M \cdot \vec{v}_S = -f_S \rho_S (C_S - C_L) \nabla \cdot \vec{v}_S + \rho_S \vec{v}_S C_L \cdot \nabla f_S \\ - f_L \rho_L \vec{v}_L \cdot \nabla C_L + \nabla (f_L \rho_L C_L) \cdot \vec{v}_S. \quad [A10]$$

Applying the chain rule on the last term of Eq. [A10] results in

$$\nabla \tilde{C}_M \cdot \vec{v}_S = -f_S \rho_S (C_S - C_L) \nabla \cdot \vec{v}_S + \rho_S \vec{v}_S C_L \cdot \nabla f_S \\ - f_L \rho_L \vec{v}_L \cdot \nabla C_L + \vec{v}_S C_L \cdot \nabla (f_L \rho_L) + f_L \rho_L \vec{v}_S \cdot \nabla C_L, \quad [A11]$$

which is equivalent to

$$\nabla \tilde{C}_M \cdot \vec{v}_S = -f_S \rho_S (C_S - C_L) \nabla \cdot \vec{v}_S + \vec{v}_S C_L \cdot \nabla (f_S \rho_S + f_L \rho_L) \\ - f_L \rho_L (\vec{v}_L - \vec{v}_S) \cdot \nabla C_L. \quad [A12]$$

Since the densities ρ_S and ρ_L are different but constant and $f_L = 1 - f_S$, the following simplification can be made:

$$\nabla (f_S \rho_S + f_L \rho_L) = (\rho_S - \rho_L) \nabla f_S. \quad [A13]$$

Hence, one can write Eq. [A12] as

$$\nabla \tilde{C}_M \cdot \vec{v}_S = f_S \rho_S (C_L - C_S) \nabla \cdot \vec{v}_S$$
$$+ \vec{v}_S C_L (\rho_S - \rho_L) \cdot \nabla f_S - f_L \rho_L (\vec{v}_L - \vec{v}_S) \cdot \nabla C_L. \quad [A14]$$

NOMENCLATURE

A_{SL}	Surface area of the cylindrical dendrites (mm^2)
C_L	Species concentration in the liquid phase (wt pct)
C_S	Species concentration in the solid phase (wt pct)
C_L^*	Species concentration in the liquid at the solidification interface (wt pct)
C_S^*	Species concentration in the solid at the solidification interface (wt pct)
C_L^C	Concentration of carbon in the liquid (wt pct)
$C_{L,0}^C$	Initial carbon concentration in the melt (liquid phase) (wt pct)
C_S^C	Concentration of carbon in the solid (wt pct)
$C_{S,E}^C$	Eutectic carbon concentration (wt pct)
C_M^C	Mixture concentration of carbon (wt pct)
$\tilde{C}_M$	Volume specific mixture concentration (kg m^{-3})
C_{LS}^D	Diffusive species transfer rate from liquid to solid (kg m^{-3} s)
C_{SL}^D	Diffusive species transfer rate from solid to liquid (kg m^{-3} s)
C_{LS}^M	Species transfer due to phase change from liquid to solid (kg m^{-3} s)
C_{SL}^M	Species transfer due to phase change from solid to liquid (kg m^{-3} s)
D_L	Diffusion coefficient of the liquid phase (m^2 s^{-1})
H^*	Volumetric heat transfer coefficient (W m^{-3} K)
ΔH_m	Latent heat of fusion (J kg^{-1})
K	Permeability of the mushy zone (mm^2)
Q_{LS}^D	Energy exchange from liquid to solid due to heat transfer (J m^{-3} s)
Q_{SL}^D	Energy exchange from solid to liquid due to heat transfer (J m^{-3} s)
Q_L^M	Phase change energy of the liquid (J m^{-3} s)
Q_S^M	Phase change energy of the solid (J m^{-3} s)
M_{LS}	Net mass transfer rate from the liquid to the solid (kg s^{-1})
M_{SL}	Net mass transfer rate from the solid to the liquid (kg s^{-1})
$S_{V,T}$	Ratio between dendritic surface area and total phase volume (mm^{-1})
T_L	Temperature of the liquid phase (K)
T_S	Temperature of the solid phase (K)
T^{envi}	Temperature of the strand environment (K)
T^{cast}	Casting temperature (initial melt temperature) (K)
T_m^{Fe}	Melting temperature of pure iron (K)
$\vec{V}_{LS}^M$	Momentum exchange due to the phase change from liquid to solid (kg m^{-2} s^{-2})
$\vec{V}_{LS}^D$	Momentum exchange due to drag force (kg m^{-2} s^{-2})
V_T	Total volume of the solid and the liquid (mm^3)
a, b	Empirical constants (−)
$c_{p,L}$	Specific heat capacity of the liquid phase (J kg^{-1} K^{-1})
$c_{p,S}$	Specific heat capacity of the solid phase (J kg^{-1} K^{-1})
d_0	Initial bulging height (mm)
f_L	Volume fraction of the liquid phase (−)
$f_{L,0}$	Initial liquid fraction (−)
f_S	Volume fraction of the solid phase (−)
f_S^{SPM}	Solid fraction for SPM calculations (−)
f_S^{zero}	Zero-strength solid fraction (−)
$\vec{g}$	Gravity acceleration (m s^{-2})
h	Distance between guiding rolls (mm)
h_L	Enthalpy of the liquid phase (J kg^{-1})
h_S	Enthalpy of the solid phase (J kg^{-1})
k	Partition coefficient (−)
k_L	Thermal conductivity of the liquid (W m^{-1} K^{-1})
k_S	Thermal conductivity of the solid (W m^{-1} K^{-1})
l	Strand length (mm)
m	Slope of the liquidus line in the linearized Fe–C phase diagram (K wt pct^{-1})
n	Total number of rolls (−)
p	Melt pressure (N mm^{-2})
p^{envi}	Pressure of the strand environment (atmospheric pressure) (K)
q	Mold length (mm)
r_1	Dendrite trunk radius (mm)
r_∞	Maximum dendrite radius (mm)
s	Strand thickness reduction due to MSR (mm)
t	Time (s)
$\vec{v}_S$	Velocity vector of the solid phase (mm s^{-1})
$\vec{v}_L$	Velocity vector of the liquid phase (mm s^{-1})
v^{cast}	Casting velocity (mm s^{-1})
v^{pull}	Pull velocity (mm s^{-1})
$v_{S,x}$	Internal solid phase velocity parallel to the cast direction (mm s^{-1})
$v_{S,y}$	Internal solid phase velocity perpendicular to the cast direction (mm s^{-1})
$v_{S,x}^{surf}$	Strand surface velocity parallel to the cast direction (mm s^{-1})
$v_{S,y}^{surf}$	Strand surface velocity perpendicular to the cast direction (mm s^{-1})
v_{r_1}	Growth velocity of the dendrites in their thickness direction (mm s^{-1})
w	Overall strand thickness (mm)
x	Strand coordinate parallel to the cast direction (mm)
x_{-1}	Melt meniscus coordinate (mm)
x_0	Bulging start coordinate (mm)
x_1	MSR start coordinate (mm)
x_2	Bulging & MSR end coordinate (mm)
x_3	Strand end coordinate (mm)
y	Strand coordinate perpendicular to the cast direction (mm)
y^{surf}	Strand surface coordinate perpendicular to the cast direction (mm)
Φ	Impingement factor to consider dendritic overlapping (−)
γ	MSR efficiency factor (−)
η_L	Dynamic viscosity of the melt (kg m^{-1} s^{-1})
λ_1	Primary dendrite arm spacing (mm)
ρ_L	Density of the liquid phase (kg m^{-3})

ρ_S Density of the solid phase (kg m^{-3})
$\bar{\rho}_S$ Average density of the solid phase (kg m^{-3})

REFERENCES

1. K. Schwerdtfeger: *Metallurgie des Stranggießens: Gießen und Erstarren von Stahl*, Verlag Stahleisen, Düsseldorf, Germany, 1992.
2. R. Thome and K. Harste: *Steel Res. Int.*, 2004, vol. 75, pp. 693–700.
3. R. Thome and K. Harste: *ISIJ Int.*, 2006, vol. 46, pp. 1839–44.
4. W. Bleck, W. Wang, and R. Bülte: *Steel Res. Int.*, 2006, vol. 77, pp. 485–91.
5. H. Preßlinger, S. Ilie, P. Reisinger, A. Schiefermüller, A. Pissenberger, E. Parteder, and C. Bernhard: *ISIJ Int.*, 2006, vol. 46, pp. 1845–51.
6. O. Bode, K. Schwerdtfeger, H.G. Geck, and F. Höfer: *Ironmak. Steelmak.*, 2008, vol. 35, pp. 137–45.
7. S. Ogibayashi, M. Kobayashi, M. Yamada, and T. Mukai: *ISIJ Int.*, 1991, vol. 31, pp. 1400–07.
8. C. Beckermann: *ASM Handbook, Volume 15: Casting*, ASM International, Materials Park, OH, 2008, pp. 348–52.
9. C. Beckermann: *Int. Mater. Rev.*, 2002, vol. 47, pp. 243–61.
10. M.C. Flemings and G.E. Nereo: *Trans. Metall. Soc. AIME*, 1967, vol. 239, pp. 1449–61.
11. M.C. Flemings, R. Mehrabian, and G.E. Nereo: *Trans. Metall. Soc. AIME*, 1968, vol. 242, pp. 41–49.
12. M.C. Flemings and G.E. Nereo: *Trans. Metall. Soc. AIME*, 1968, vol. 242, pp. 50–55.
13. K. Miyazawa and K. Schwerdtfeger: *Arch. Eisenhüttenwesen*, 1981, vol. 52, pp. 415–22.
14. P. Stadler, K. Hagen, P. Hammerschmid, and K. Schwerdtfeger: *Stahleisen*, 1982, vol. 102, pp. 451–59.
15. T. Kajitani, J.-M. Drezet, and M. Rappaz: *Metall. Mater. Trans. A*, 2001, vol. 32A, pp. 1479–91.
16. G. Lesoult: *Mater. Sci. Eng. A*, 2005, vols. 413–414, pp. 19–29.
17. F. Mayer, M. Wu, and A. Ludwig: in *Modeling of Casting, Welding and Advanced Solidification Processes XII*, S.L. Cockcroft and D.M. Maijer, eds., TMS, Warrendale, PA, 2009, pp. 279–86.
18. F. Mayer, M. Wu, and A. Ludwig: *Steel Res. Int.*, 2010, vol. 81, pp. 660–67.
19. M. Wu, J. Domitner, and A. Ludwig: *Metall. Mater. Trans. A*, 2012, vol. 43A, pp. 945–64.
20. A. Ludwig and M. Wu: *Mater. Sci. Eng. A*, 2005, vols. 413–414, pp. 109–14.
21. M. Wu and A. Ludwig: *Metall. Mater. Trans. A*, 2006, vol. 37A, pp. 1613–31.
22. M. Wu and A. Ludwig: *Metall. Mater. Trans. A*, 2007, vol. 38A, pp. 1465–75.
23. J. Ni and C. Beckermann: *Metall. Trans. B*, 1991, vol. 22B, pp. 349–61.
24. C. Beckermann and R. Viskanta: *Appl. Mech. Rev.*, 1993, vol. 46, pp. 1–27.
25. M.C. Schneider, J.P. Gu, C. Beckermann, W.J. Boettinger, and U.R. Kattner: *Metall. Mater. Trans. A*, 1997, vol. 28A, pp. 1517–31.
26. A.K. Dahle and D.H. StJohn: *Acta Mater.*, 1999, vol. 47, pp. 31–41.
27. J. Domitner, J.-M. Drezet, M. Wu, and A. Ludwig: *IOP*, 2012, vol. 33, p. 012058.
28. N.N.: voestalpine Stahl GmbH, Linz (unpublished research).